Research Square

Preprints are preliminary reports that have not undergone peer review.
They should not be considered conclusive, used to inform clinical practice,
or referenced by the media as validated information.

Functional Reprogramming of a Marine Natural Product Enables Broad-Spectrum Anti- Pyroptotic Therapy for Intervertebral Disc Degeneration

Wei Li[1]
Shanghai University
Linhui Han[2]
The Second Affiliated Hospital of Naval Medical University
Wenbo Lin[2]
The Second Affiliated Hospital of Naval Medical University
Tingfei Yan[2]
The Second Affiliated Hospital of Naval Medical University
Rui Zhang[2]
Shanghai University
Xiaowei Luan[3]
Shanghai University
Jialin Li
Shanghai University
Haisong Yang
yangspine@163.com
Shanghai University

Research Article

Keywords: Intervertebral disc degeneration, Pyroptosis, NLRP3 inflammasome, Functional reprogramming, Redox regulation, Biomimetic nanomedicine

Posted Date: November 16th, 2026

DOI: https://doi.org/10.21203/rs.3.rs-11424447/v1

License: This work is licensed under a Creative Commons Attribution 4.0 International License.
Read Full License

Additional Declarations: No competing interests reported.

Abstract

Background

Pyroptosis contributes to intervertebral disc degeneration, yet its interplay with oxidative stress may limit the efficacy of single-target interventions. This study aimed to identify a marine-derived anti-pyroptotic compound and expand its therapeutic potential through functional reprogramming.

Results

Single-cell transcriptomic analysis of human nucleus pulposus tissues revealed state-dependent enrichment of pyroptosis-associated programs during cellular remodeling, highlighting NLRP3 as a potential therapeutic target. Phenotype-based screening of marine natural products identified 5-[(1H-indol-3-yl) methylidene] imidazolidine-2,4-dione (IMH) as a selective inhibitor of NLRP3-associated pyroptosis. Multidimensional target validation confirmed direct IMH–NLRP3 binding and identified key residues contributing to their interaction. To overcome the pathway selectivity and limited antioxidant capacity of IMH, we functionally reprogrammed it into ruthenium-containing carbon dots and introduced platelet/nucleus pulposus cell hybrid membrane camouflage, generating Fm-IMH-CDs. This reprogramming preserved NLRP3 engagement while conferring multienzyme-mimetic regulation of reactive oxygen species and preferential recognition of pyroptotic nucleus pulposus cells. Fm-IMH-CDs suppressed oxidative stress, mitochondrial dysfunction, inflammatory signaling, and pyroptotic injury across multiple inflammatory contexts, accompanied by modulation of NOD-like receptor and nuclear factor κB signaling. In a rat model of intervertebral disc degeneration, Fm-IMH-CDs prolonged intradiscal retention, preserved nucleus pulposus architecture and extracellular matrix, reduced pyroptosis-associated inflammation and matrix catabolism, and attenuated disc degeneration.

Conclusions

Functional reprogramming transforms a pathway-selective marine natural product into a multifunctional biomimetic nanoplatform integrating molecular targeting, redox regulation, and preferential cellular recognition. This strategy offers a promising approach for broader anti-pyroptotic intervention in intervertebral disc degeneration.

Introduction

Intervertebral disc degeneration (IVDD) is one of the most common structural manifestations of spinal aging and degeneration and is closely associated with a range of clinical conditions, including low back pain, disc herniation, spinal stenosis, and segmental instability[1,2]. Current management of IVDD primarily relies on rehabilitation, analgesic medications, and surgical intervention[3]. Although these treatments can alleviate pain, decompress neural structures, or restore local mechanical stability, they generally fail to

reverse the underlying biological processes of disc degeneration[4]. Given the lack of clinically established pharmacological therapies capable of directly modifying IVDD progression, elucidating the key cellular and molecular mechanisms underlying disc degeneration and developing mechanism-based therapeutic strategies remain of considerable clinical and translational importance.

The nucleus pulposus (NP) is essential for maintaining intervertebral disc homeostasis, with nucleus pulposus cells (NPCs) sustaining the proteoglycan-rich extracellular matrix (ECM) required for tissue function[5,6]. IVDD progression involves ECM degradation, inflammatory activation, oxidative imbalance, and profound alterations in NPC phenotype and cell fate[1]. Recent single-cell transcriptomic studies have further revealed substantial heterogeneity among NPC populations and dynamic cellular-state remodeling during degeneration, suggesting that specific NPC states may contribute to disease progression[6,7]. Among various regulated cell-death pathways, pyroptosis has emerged as an important mechanism linking cellular loss to inflammatory amplification[8]. NLRP3 inflammasome-mediated pyroptosis, characterized by Caspase-1 activation, GSDMD cleavage, and inflammatory cytokine release, has been implicated in IVDD and other degenerative diseases[8,9]. Importantly, ROS accumulation and mitochondrial dysfunction serve as critical upstream signals promoting NLRP3 activation and can further amplify inflammatory injury[10]. Although ROS/NLRP3 and NLRP3/Caspase-1 pathways have been associated with NPC damage and ECM degradation[11,12], how pyroptosis programs evolve during NPC state transitions and whether targeting NLRP3 alone is sufficient to overcome the oxidative degenerative microenvironment remain unclear.

Notably, pyroptosis is not a uniform cell-death program governed exclusively by NLRP3 inflammasome activation, but rather represents a convergent inflammatory process that can be initiated through multiple upstream sensing mechanisms[13]. In addition to the canonical NLRP3-Caspase-1-GSDMD axis, other inflammasomes, including AIM2 and NLRC4, can activate Caspase-1-dependent pyroptosis in response to distinct danger signals[14,15]. Moreover, noncanonical inflammasome signaling can be initiated by cytosolic lipopolysaccharide through inflammatory caspases, which subsequently promotes GSDMD-mediated membrane permeabilization and can secondarily amplify canonical inflammasome activation[16]. Importantly, oxidative stress constitutes an additional layer of pyroptotic regulation rather than merely an upstream trigger of NLRP3[17–19]. Excessive ROS accumulation, mitochondrial dysfunction, and impaired redox homeostasis can promote inflammasome activation, perturb intracellular signaling, and lower the threshold for inflammatory cell death, thereby creating a feed-forward relationship between oxidative injury and pyroptosis[10,19]. Thus, in the degenerative intervertebral disc microenvironment, where mechanical stress, mitochondrial dysfunction, chronic inflammation, and redox imbalance coexist, pyroptosis is likely sustained by convergent and mutually reinforcing signaling routes rather than by a single inflammasome pathway[20]. This networked nature of pyroptotic activation raises an important therapeutic consideration: selective inhibition of one inflammasome, although mechanistically effective, may leave parallel pyroptotic routes and the upstream oxidative stress that continuously fuels them largely unaddressed. A broader anti-pyroptotic strategy capable of

simultaneously intercepting multiple activation routes and restoring the pathological redox environment may therefore provide a more comprehensive means of suppressing inflammatory cell death and interrupting the self-amplifying cycle of oxidative stress, inflammation, and tissue degeneration.

Therefore, we reasoned that effective anti-pyroptotic therapy should extend beyond single-node inhibition by simultaneously targeting a key pyroptotic pathway and the oxidative microenvironment that amplifies inflammatory cell death. Marine natural products provide a rich source of structurally diverse anti-inflammatory molecules, yet their therapeutic efficacy may be limited when restricted to a single molecular target. In this study, we identified IMH, an NLRP3-targeting marine natural product, as a selective anti-pyroptotic compound through phenotype-based screening. To overcome its limited intrinsic ROS-regulatory capacity, we developed a functional reprogramming strategy by integrating Ru-mediated carbon-dot engineering to introduce multienzyme-mimetic antioxidant activity while preserving NLRP3 targeting. The resulting Fm-IMH-CDs were further equipped with platelet/NPC hybrid biomimetic membranes to enhance pathological-cell interaction and local retention. By integrating NLRP3 inhibition with ROS regulation, this strategy transformed a pathway-selective small molecule into a multifunctional anti-pyroptotic platform, enabling coordinated modulation of pyroptosis, oxidative stress, inflammation, and ECM degeneration in IVDD.

Results

Single-cell transcriptomic analysis reveals enhanced pyroptosis-associated programs in NPCs during IVDD progression

IVDD is characterized by disruption of extracellular matrix (ECM) homeostasis, inflammation, oxidative stress, and alterations in NPC phenotype and cell fate[21–23]. Previous single-cell studies have further revealed substantial cellular heterogeneity within human nucleus pulposus (NP) tissues and dynamic remodeling of NPC states during degeneration[24,25]. To characterize pyroptosis-associated alterations at single-cell resolution, we reanalyzed the publicly available scRNA-seq dataset GSE165722, which includes human NP tissues with different degrees of degeneration[26]. Based on the expression of canonical marker genes, seven major cell populations were identified, including neutrophils (e.g., *FCGR3B, CXCR1*, and *FPR1*), NPCs (e.g., *HAPLN1, ASPN*, and *CNMD*), T cells (e.g., *CD3D, CD3G*, and *CD2*), macrophages (e.g., *C1QA, C1QC*, and *FOLR2*), erythroid cells (e.g., *GYPA, SLC4A1*, and *ALAS2*), B cells (e.g., *MS4A1, CD79A*, and *IGHM*), and endothelial cells (e.g., *EMCN, KDR*, and *CLEC14A*) (Fig. 1A and Fig. S1). Their relative proportions varied substantially across degeneration stages, indicating broad remodeling of the NP cellular landscape (Fig. 1B). Because NPCs are the principal resident cells responsible for maintaining NP matrix homeostasis[27], we next extracted NPCs for subclustering analysis. Six NPC subpopulations were identified: Met_NPCs, Effector_NPCs, Degenerative_NPCs, Adh_NPCs, Homeostatic_NPCs, and Fibro_NPCs (Fig. 1C, D). Their distribution changed markedly with degeneration. Met_NPCs predominated in less degenerated tissues but declined substantially in severe

degeneration, whereas Effector_NPCs, Degenerative_NPCs, and Adh_NPCs were relatively enriched (Fig. 1E). These findings indicate pronounced remodeling of NPC-state composition during IVDD progression.

We next examined whether NPC state remodeling was accompanied by alterations in pyroptosis-associated transcriptional programs. Using a curated pyroptosis-related gene set, we calculated pyroptosis scores for individual NPCs. Notably, pyroptosis scores were preferentially elevated in the mildly degenerated group (Fig. 1F). This pattern suggests that pyroptosis-associated programs may be activated relatively early during IVDD progression, potentially contributing to the initiation of pathological NPC state transitions. Further, we integrated pseudotime trajectory inference with CytoTRACE analysis. Pyroptosis scores changed dynamically along the inferred NPC trajectory and showed an overall increase toward later pseudotime states (Fig. 1G). Stratification by degeneration stage revealed distinct pyroptosis-score trajectories among the normal, mildly degenerated, and severely degenerated groups (Fig. 1H), whereas analysis across NPC subpopulations demonstrated marked subtype-dependent differences (Fig. 1I). Consistent with these trajectory-level observations, late-state NPCs exhibited higher pyroptosis scores than early-state NPCs (Fig. 1J). CytoTRACE analysis further revealed differences in predicted cellular differentiation potential across NPC states (Fig. 1K). Mapping of NPC subpopulations onto the inferred cellular-state landscape demonstrated an ordered distribution of distinct NPC phenotypes (Fig. 1L, N), while correlation analysis identified genes associated with CytoTRACE-defined state progression (Fig. 1M). Notably, several inflammation- and degeneration-associated genes showed positive correlations with CytoTRACE scores, supporting progressive transcriptional remodeling during NPC state transition. In parallel, feature-plot analysis showed state-dependent expression of the pyroptosis-associated genes *NLRP3* and *CASP1* across NPC populations (Fig. 1O). Given the established role of the NLRP3 inflammasome in Caspase-1-dependent pyroptosis[28] and its involvement in disc inflammation and ECM degeneration[29], these findings suggest that NLRP3-associated pyroptotic programs progressively accumulate in degeneration-associated NPC states.

We next validated these molecular alterations in human intervertebral disc tissues representing different degrees of degeneration. Representative T2-weighted MRI images illustrated the radiological features of mildly and severely degenerated intervertebral discs (Fig. 1P). Compared with mildly degenerated tissues, severely degenerated tissues exhibited markedly increased MMP3 staining, indicating enhanced ECM catabolism, together with higher proportions of NLRP3- and cleaved-Caspase-1-positive cells (Fig. 1Q-R). These histological findings corroborated the single-cell transcriptomic results and supported enhanced NLRP3/Caspase-1-associated pyroptotic features in severe IVDD.

Collectively, single-cell analysis revealed pronounced remodeling of NPC states during IVDD progression. Rather than increasing simply with clinical degeneration grade, pyroptosis-associated programs became progressively enriched along degeneration-associated NPC-state transitions, accompanied by increased NLRP3/CASP1-related features. Human tissue validation further confirmed enhanced ECM catabolism and NLRP3/Caspase-1-associated pyroptotic activity in severe degeneration. Together, these findings

identify NPC-state remodeling and NLRP3-associated pyroptosis as interconnected pathological features of IVDD and provide a rationale for subsequent NLRP3-targeted intervention.

Marine natural product screening identifies IMH as a selective inhibitor of NLRP3-associated pyroptosis

Given the enhanced NLRP3-associated pyroptotic features observed during IVDD progression, we performed phenotype-based screening of a marine natural product library to identify compounds with anti-pyroptotic activity. NPCs were primed with LPS and subsequently stimulated with ATP, with cell viability assessed by CCK-8 as the primary screening readout (Fig. 2A). Initial screening identified several compounds with protective effects against LPS/ATP-induced NPC injury. Among them, 5-[(1H-indol-3-yl)methylidene]imidazolidine-2,4-dione (IMH), 2,5-dihydroxybenzaldehyde, and 3,3'-bi(1H-indole) showed the most pronounced cytoprotective activity and were selected for secondary evaluation (Fig. 2B). Concentration–response analysis further demonstrated that IMH produced the most consistent and prominent dose-dependent restoration of cell viability, including at relatively low concentrations (Fig. 2C), and was therefore selected as the lead candidate (Fig. 2D). Using MCC950 as a reference NLRP3 inhibitor, the apparent EC50 values of IMH and MCC950 were approximately 1.0 μM and 3.01 μM, respectively (Fig. 2E), indicating potent cytoprotective activity of IMH in the low-micromolar range.

We next determined whether the protective effect of IMH was associated with suppression of pyroptotic cell death. LPS/ATP stimulation markedly increased FAM-FLICA/PI double-positive cells, whereas IMH substantially reduced this population, with an effect comparable to MCC950 (Fig. 2F). Consistently, IMH markedly reduced PI uptake induced by LPS/ATP stimulation (Fig. 2G, H), indicating preservation of plasma membrane integrity. These results support a pronounced inhibitory effect of IMH on Caspase-1-associated pyroptotic cell death. To determine whether this protective effect was restricted to NPCs, we further evaluated IMH in rat NPCs, rat endplate cells, BMSCs, and BMDMs. Across these cell types, inflammatory stimulation reduced cell viability and increased LDH release, whereas IMH treatment restored viability and reduced LDH release in a concentration-dependent manner (Fig. 2I-L). Thus, the cytoprotective effect of IMH against inflammasome-associated lytic cell death was reproducible across multiple cell types.

We next examined the pathway selectivity of IMH. IMH markedly protected cells against LPS/nigericin-induced injury in a concentration-dependent manner (Fig. S2). In contrast, only partial protection was observed at the highest IMH concentration under poly(dA:dT) stimulation, while no significant protection was detected following flagellin or Pam3CSK4 stimulation (Fig. S2). Because ATP and nigericin are commonly used to activate NLRP3, whereas poly(dA:dT) and flagellin activate AIM2- and NLRC4-associated inflammasome pathways, respectively, these findings indicate that IMH preferentially suppresses NLRP3-associated pyroptotic injury rather than broadly inhibiting diverse inflammatory pathways.

Multidimensional target validation reveals that IMH directly binds to NLRP3 and enhances its protein stability

Given the preferential protective activity of IMH under NLRP3-activating conditions, we next investigated whether NLRP3 represents a direct molecular target of IMH. Molecular docking was first performed against a panel of pyroptosis-related proteins, including NLRP3, NEK7, AIM2, GSDMD, CASP1, Pyrin, NINJ1, and NLRC4 (Fig. 3A). Among these candidates, NLRP3 showed the most favorable predicted binding score for IMH (-7.121) (Fig. 3B). Structural analysis suggested that IMH occupies a putative pocket within NLRP3 and interacts with surrounding residues through multiple non-covalent interactions, including hydrophobic interactions and π–π stacking (Fig. 3C).

We next performed a 100-ns molecular dynamics (MD) simulation to evaluate the stability and conformational behavior of the IMH–NLRP3 complex. RMSD analysis indicated that the complex reached a relatively stable conformational state during the simulation (Fig. 3D, E), while SASA and radius of gyration (Rg) analyses showed no substantial changes in overall compactness or solvent exposure (Fig. 3F, H). Gibbs free-energy landscape, RMSF, and hydrogen-bond analyses further supported a dynamically stable IMH–NLRP3 interaction (Fig. 3G, I, and K). MM-PBSA analysis estimated a favorable binding free energy of approximately − 30 kcal/mol, with van der Waals and nonpolar interactions providing major energetic contributions (Fig. S3). Per-residue energy decomposition further highlighted several candidate residues contributing to the predicted binding interface, includingM578, M661, I411, F410, M408, Y632, T659, and V414 (Fig. S3).

We next experimentally validated the predicted interaction. Surface plasmon resonance (SPR) showed concentration-dependent binding of IMH to NLRP3, with an equilibrium dissociation constant (K_D) of 2.28×10^{-5} M (Fig. 3L). These results provide direct biophysical evidence of IMH–NLRP3 binding. Consistently, drug affinity responsive target stability (DARTS) assays showed that IMH protected endogenous NLRP3 from Pronase-mediated proteolysis in a concentration-dependent manner (Fig. 3M). This protection was reproduced using recombinant NLRP3 protein (Fig. 3N), supporting a direct interaction independent of the intracellular environment. Cellular thermal shift assays (CETSA) further demonstrated that IMH increased the thermal stability of endogenous and recombinant NLRP3, producing thermal shifts of approximately 3.1 and 9.0°C, respectively (Fig. 3O, P). Together, these complementary assays establish direct target engagement between IMH and NLRP3.

To further define the IMH-binding interface, candidate residues predicted by the computational analyses were subjected to site-directed mutagenesis. DARTS analysis showed that the M661A mutation markedly impaired IMH-mediated stabilization of NLRP3 compared with wild-type protein (Fig. 3Q). Additional mutations at M578, Y632, and I411 also altered IMH-induced NLRP3 stabilization to varying degrees (Fig. 3R, S), supporting the involvement of a defined multi-residue binding interface, with M661 emerging as a major contributor to IMH recognition. Functional validation further showed that mutation of the identified binding site markedly attenuated the ability of IMH to restore cell viability and reduce LDH release under pyroptotic stimulation (Fig. S4). Moreover, the protective effect of IMH progressively

diminished after compound washout (Fig. S5), consistent with the predominantly reversible, non-covalent interactions predicted by the structural analyses.

Collectively, these results identify NLRP3 as a direct molecular target of IMH. These findings establish a molecular basis for the preferential inhibition of NLRP3-associated pyroptosis by IMH and provide the mechanistic foundation for its subsequent functional reprogramming.

Preparation and Characterization of Fm-IMH-CDs

Although IMH directly targets NLRP3, pyroptotic injury in IVDD is unlikely to be driven by a single molecular event. Oxidative stress and excessive ROS accumulation are prominent features of the degenerative disc microenvironment and can amplify inflammasome activation and other types of pyroptosis[11]. We therefore evaluated the intrinsic antioxidant capacity of IMH. IMH exhibited weak SOD- and CAT-like activity (Fig. S6), indicating that its intrinsic antioxidant capacity is limited. Thus, although IMH directly targets NLRP3, it is unlikely to provide sufficient redox regulation to counteract the complex oxidative stress associated with IVDD, highlighting the need to expand its antioxidant functionality.

To overcome this limitation, we sought to functionally reprogram IMH while preserving its NLRP3-targeting activity and introducing additional ROS-regulatory capacity. Precursor-derived carbon dots can retain bioactive features of their molecular precursors while acquiring new redox properties during carbonization[30,31], whereas redox-active metal centers can provide enzyme-mimetic catalytic functions[32]. We therefore employed Ru-mediated carbon-dot engineering. In addition, we introduced a hybrid biomimetic membrane to enhance preferential delivery to pyroptotic NPCs. Pyroptotic NPCs release abundant inflammatory mediators, creating a highly inflammatory local microenvironment that provides a pathological cue for targeted recognition. Given the intrinsic inflammation-homing properties of platelets[33,34], platelet membranes were incorporated to recognize the pathological state. Meanwhile, NPC-derived membranes can confer homotypic recognition toward NPCs[35]. We therefore fused platelet and NPC membranes to integrate inflammation-directed tropism with NPC-specific recognition within a single biomimetic interface[36], thereby facilitating preferential interaction of IMH-CDs with pyroptotic NPCs. Thus, Fm-IMH-CDs was developed.

As the results show, Fm-IMH-CDs were fabricated through a two-stage synthesis and biomimetic assembly strategy (Fig. 4A). First, IMH and $RuCl_3$ were subjected to solvothermal treatment at 180°C for 8 h, followed by dialysis to obtain Ru-containing IMH-derived carbon dots, hereafter referred to as IMH-CDs. In parallel, Ru-free IMH-derived carbon dots were prepared under otherwise identical conditions in the absence of $RuCl_3$ and are hereafter referred to as CDs. Platelet and NPC membranes were separately isolated and fused to form a hybrid membrane, which was subsequently coated onto IMH-CDs to generate Fm-IMH-CDs. Transmission electron microscopy revealed uniformly dispersed ultrasmall nanostructures with diameters of approximately 9 nm (Fig. 4B, C). Dynamic light scattering showed a narrow size distribution centered at 9.106 nm with a polydispersity index of 0.1438, while the zeta

potential was + 26.24 mV (Fig. 4D, E). XRD showed a broad diffraction feature consistent with a predominantly amorphous carbon framework (Fig. 4F). XPS confirmed the presence of C, O, and Ru (Fig. 4G). High-resolution spectra further revealed C-C, C-O, and C = O components in the C 1s region, multiple Ru oxidation states including Ru^{3+} and Ru^{4+}, and several oxygen-containing surface groups (Fig. 4H-J), supporting successful formation of Ru-containing IMH-derived carbon nanostructures. Cryo-TEM further demonstrated a continuous membrane-like shell surrounding the nanoparticle core of Fm-IMH-CDs (Fig. 4K, L). Coomassie brilliant blue staining showed preservation of the overall membrane protein profile, while Western blotting confirmed the presence of both the platelet marker CD41 and the NPC-associated marker CD24 in the final formulation (Fig. 4M). These findings support successful hybrid membrane coating with retention of representative protein components from both source membranes.

We next investigated whether hybrid membrane camouflage conferred preferential targeting toward pyroptotic NPCs (Fig. 4N, O). Compared with NPC membrane-coated IMH-CDs (m-IMH-CDs), Fm-IMH-CDs exhibited markedly enhanced cellular association with pyroptotic NPCs. Notably, suppression of NLRP3-dependent pyroptotic signaling by MCC950 substantially reduced the accumulation of Fm-IMH-CDs in pyroptotic NPCs, indicating that the enhanced recognition was closely associated with the pyroptotic cell state. In contrast, both m-IMH-CDs and Fm-IMH-CDs exhibited minimal association with heterotypic BMDMs, with no significant difference between the two formulations. Collectively, these findings suggest that hybrid membrane functionalization endows Fm-IMH-CDs with preferential recognition of pyroptotic NPCs while maintaining low nonspecific association with heterotypic cells.

Collectively, these results establish Fm-IMH-CDs as a Ru-containing IMH-derived carbon-dot platform coated with a platelet/NPC hybrid membrane. The formulation retained representative membrane proteins from both source cells and exhibited preferential interaction with pyroptotic NPCs, providing a structural and delivery basis for subsequent evaluation of its ROS-regulatory and anti-pyroptotic functions.

Enzyme-Mimetic Activities and Mechanistic Analysis of Fm-IMH-CDs

Having established the structural characteristics of Fm-IMH-CDs, we next investigated whether Ru incorporation endowed the carbon-dot core with enhanced ROS-regulatory activity. CDs exhibited relatively weak Trolox-equivalent antioxidant capacity, whereas Ru incorporation markedly enhanced the antioxidant response in a concentration-dependent manner (Fig. 5A). Consistently, Ru-containing IMH-CDs displayed pronounced SOD-like activity, inhibiting approximately 90% of formazan formation compared with approximately 35% for Ru-free CDs (Fig. 5B). Ru incorporation also substantially enhanced CAT-like activity, resulting in approximately 90% H_2O_2 decomposition, whereas Ru-free CDs showed minimal activity (Fig. 5C). Similarly, GPx-like activity increased from nearly undetectable levels in CDs to approximately 23 active units after Ru incorporation (Fig. 5D). Hybrid membrane coating largely

preserved these antioxidant and multienzyme-mimetic activities. Together, these results identify Ru incorporation as the principal contributor to the enhanced SOD-, CAT-, and GPx-like catalytic functions of Fm-IMH-CDs.

To investigate the mechanistic basis of this catalytic enhancement, structural models of Ru-free and Ru-containing IMH-derived carbon dots were constructed (Fig. 5E), followed by density functional theory calculations of the proposed GPx-, SOD-, and CAT-like catalytic pathways. In the GPx-like pathway, the Ru-containing structure facilitated H_2O_2 activation and subsequent transformation of oxygenated intermediates involved in thiol oxidation (Fig. 5F). The corresponding energy profile indicated that Ru incorporation altered the energetics of key intermediate transformations, rendering the overall catalytic process more favorable than that of the Ru-free model (Fig. 5G). A similar effect was observed for the SOD-like pathway. Ru-containing catalytic sites facilitated the adsorption and conversion of hydroperoxyl intermediates and subsequent O_2 formation (Fig. 5H), with a more favorable energetic profile than the Ru-free carbon-dot model (Fig. 5I). For the CAT-like pathway, H_2O_2 adsorption and decomposition proceeded through sequential oxygen-containing surface intermediates followed by H_2O and O_2 generation and regeneration of the catalytic surface (Fig. 5J). Ru incorporation substantially redistributed the energetics of these intermediate states and favored H_2O_2 conversion (Fig. 5K).

Collectively, the experimental and theoretical analyses demonstrate that Ru incorporation functionally reprograms IMH-derived carbon dots into a multifunctional nanozyme with enhanced SOD-, CAT-, and GPx-like activities. Importantly, these catalytic functions were retained after hybrid membrane coating, establishing Fm-IMH-CDs as a biomimetic nanoplatform that integrates multienzyme-mimetic ROS regulation with the preferential cellular interaction demonstrated above.

Fm-IMH-CDs achieve multidimensional anti-pyroptotic effects by preserving NLRP3-targeting activity and enhancing ROS regulation

Having established the multienzyme-mimetic antioxidant activity of Fm-IMH-CDs, we next examined whether carbon-dot reprogramming preserved the NLRP3-targeting property of IMH. DARTS analysis showed that IMH-CDs protected recombinant NLRP3 from Pronase-mediated proteolysis in a concentration-dependent manner **(Fig. S8)**, indicating that the target-engagement property of IMH was retained after carbon-dot conversion.

We next evaluated whether this dual functionality translated into enhanced protection against NLRP3-associated pyroptosis. In LPS + ATP-stimulated NPCs, free IMH, IMH-CDs, and Fm-IMH-CDs all improved cell viability and reduced LDH release, with Fm-IMH-CDs showing the strongest effects **(Fig. 6A-C)**. Consistently, Fm-IMH-CDs markedly reduced PI-positive cells and alleviated the characteristic membrane damage and pyroptotic morphology induced by LPS + ATP **(Fig. 6D-F)**, demonstrating superior protection against pyroptotic membrane injury and lytic cell death. We further examined the contribution of ROS regulation. LPS + ATP stimulation induced pronounced intracellular ROS accumulation, loss of

mitochondrial membrane potential, and increased mtROS, all of which were substantially attenuated by IMH-CDs and more prominently by Fm-IMH-CDs **(Fig. 6G-L)**. Fm-IMH-CDs also significantly reduced the release of IL-1β, IL-18, and IL-6 **(Fig. 6M)**, indicating coordinated suppression of oxidative stress, mitochondrial dysfunction, and pyroptosis-associated inflammatory signaling.

Because free IMH showed preferential activity under NLRP3-activating conditions, we next examined whether functional reprogramming broadened its protective spectrum. Compared with free IMH, IMH-CDs and Fm-IMH-CDs provided greater cytoprotection under poly(dA:dT), flagellin, and Pam3CSK4 stimulation, with Fm-IMH-CDs generally exhibiting the strongest effects **(Fig. 6N)**. These findings suggest that functional reprogramming expands the activity of IMH beyond predominantly NLRP3-directed intervention toward broader regulation of inflammasome- and inflammation-associated cellular injury. To determine whether this expanded protection was dependent on ROS regulation, exogenous H_2O_2 was introduced under different inflammatory stimulation conditions. H_2O_2 supplementation markedly attenuated the cytoprotective effects of Fm-IMH-CDs following LPS + ATP, poly(dA:dT), flagellin, or Pam3CSK4 stimulation **(Fig. S9)**. These findings support ROS regulation as a major contributor to the broadened protective activity acquired after functional reprogramming, rather than the effects being attributable solely to direct NLRP3 targeting.

Collectively, carbon-dot-based functional reprogramming preserved the NLRP3-targeting property of IMH while introducing multienzyme-mimetic ROS-regulatory activity. By integrating direct NLRP3 intervention with intracellular and mitochondrial redox regulation, Fm-IMH-CDs transformed a pathway-selective small molecule into a multifunctional anti-pyroptotic nanosystem with broader protective activity across multiple inflammatory contexts.

Transcriptomic analysis reveals that Fm-IMH-CDs remodel IVDD-associated inflammatory and immune transcriptional networks

To further characterize the molecular response to Fm-IMH-CD treatment, we performed transcriptomic sequencing of the Control, IVDD, and Fm-IMH-CD-treated groups. Principal component analysis showed clear separation between the Control and IVDD groups, while the treated samples shifted away from the untreated IVDD state, indicating substantial transcriptional remodeling after treatment (Fig. 7A). Differential expression analysis identified 1,290 upregulated and 845 downregulated genes in IVDD versus Control, whereas 116 genes were upregulated and 80 were downregulated after Fm-IMH-CD treatment relative to IVDD (Fig. 7B, C). The more restricted treatment-responsive gene set suggested preferential modulation of specific disease-associated pathways rather than global reversal of the degenerative transcriptome.

Gene Ontology analysis showed that IVDD-associated genes were enriched in inflammatory responses, chemotaxis, cytokine-mediated signaling, extracellular matrix organization, and receptor-related functions (Fig. 7D-F). Genes altered by Fm-IMH-CD treatment were enriched in overlapping modules involving immune and inflammatory responses, myeloid cell-related processes, extracellular matrix

organization, and cytokine/receptor regulation (Fig. 7G-I), indicating that treatment preferentially modulated core inflammation–immunity-matrix networks associated with degeneration.

KEGG enrichment further identified multiple inflammatory and innate immune pathways, including NOD-like receptor, NF-κB, and TNF signaling (Fig. 7J). Among these, NOD-like receptor and NF-κB signaling were particularly relevant because NLRP3 belongs to the NOD-like receptor family, while NF-κB provides a major priming signal for NLRP3 inflammasome activation through transcriptional induction of NLRP3 and pro-IL-1β. GSEA confirmed significant enrichment of NOD-like receptor signaling in IVDD versus Control (ES = 0.512, NES = 1.75, P < 0.001; Fig. 7K) and a corresponding shift after treatment (ES = 0.285, NES = 1.20, P < 0.01; Fig. 7L). Similarly, NF-κB signaling was strongly enriched in IVDD (ES = 0.601, NES = 1.97, P < 0.001; Fig. 7M) and significantly altered following Fm-IMH-CD treatment (ES = 0.291, NES = 1.17, P < 0.01; Fig. 7N).

Collectively, these transcriptomic data indicate that Fm-IMH-CDs remodel disease-associated inflammatory and immune transcriptional programs, particularly NOD-like receptor- and NF-κB-related signaling. Together with the preceding evidence of direct NLRP3 targeting and ROS regulation, these findings provide systems-level support that Fm-IMH-CDs act beyond a single molecular target to modulate broader inflammatory networks relevant to IVDD.

Fm-IMH-CDs attenuate IVDD progression and pyroptosis-associated inflammation in vivo

Following the in vitro and transcriptomic analyses, we evaluated the intradiscal retention and therapeutic efficacy of Fm-IMH-CDs in a rat puncture-induced IVDD model (Fig. 8A). Cy5.5-based in vivo imaging showed progressive signal decay after intradiscal injection in all groups; however, Fm-IMH-CDs maintained substantially stronger fluorescence within the disc than free Cy5.5 or uncoated IMH-CDs at multiple time points and exhibited slower signal loss over 14 days (Fig. 8B, C). These findings indicate that platelet/NPC hybrid membrane coating enhances local retention within the intervertebral disc.

Radiological evaluation further demonstrated the therapeutic effects of Fm-IMH-CDs. The IVDD group showed reduced T2-weighted MRI signal and increased Pfirrmann scores, whereas IMH-CDs partially ameliorated these changes and Fm-IMH-CDs produced a more pronounced improvement **(Fig. 8D, E)**. Consistently, X-ray analysis showed substantial disc-height loss after puncture, which was partially restored by IMH-CDs and further improved by Fm-IMH-CDs **(Fig. 8F, G)**, indicating attenuation of structural degeneration. Histological analyses corroborated the imaging findings. H&E staining showed severe disruption of NP architecture and increased degeneration scores in the IVDD group, while Fm-IMH-CDs more effectively preserved tissue organization than uncoated IMH-CDs **(Fig. 8H, I)**. Safranin O/Fast Green staining further demonstrated pronounced disruption of the NP and surrounding matrix in the IVDD group, whereas Fm-IMH-CD treatment resulted in better preservation of the proteoglycan-rich matrix structure **(Fig. 8J)**. These findings were further supported by Alcian blue staining. Compared with the Sham group, IVDD markedly reduced Alcian blue-positive matrix, indicating substantial loss of the

proteoglycan-rich ECM. IMH-CD treatment partially restored Alcian blue staining, whereas Fm-IMH-CDs produced a further increase in the Alcian blue-positive area **(Fig. 8K, L)**. Collectively, the H&E, Safranin O/Fast Green, and Alcian blue staining results demonstrate that Fm-IMH-CDs not only preserve overall intervertebral disc architecture but also effectively attenuate ECM degeneration characterized by proteoglycan loss, further supporting their protective effects on NP tissue homeostasis.

We next examined whether the in vivo therapeutic effects were accompanied by suppression of pyroptosis-associated inflammation. Immunohistochemical analysis showed increased NLRP3, N-GSDMD, IL-1β, and MMP3 expression in degenerative discs, reflecting enhanced inflammasome/pyroptosis signaling, inflammatory activity, and matrix catabolism **(Fig. 8M, N)**. IMH-CDs reduced these pathological markers to varying degrees, whereas Fm-IMH-CDs produced more pronounced reductions in NLRP3-, N-GSDMD-, IL-1β-, and MMP3-positive cells **(Fig. 8M, N)**. These molecular changes were consistent with the preceding evidence that Fm-IMH-CDs integrate NLRP3-targeted intervention with ROS regulation to suppress pyroptotic and inflammatory injury.

Systemic biosafety was further evaluated after administration of IMH and the IMH-derived carbon-dot formulations. H&E staining of the heart, liver, spleen, lung, and kidney revealed no obvious treatment-associated histopathological abnormalities **(Fig. S10A)**. Serum biochemical indices related to hepatic, cardiac, and renal function, including AST, ALT, CK, CK-MB, LDH, CREA, urea, and UA, also showed no evident treatment-related disturbances **(Fig. S10B-I)**, supporting favorable biocompatibility under the present experimental conditions.

Collectively, Fm-IMH-CDs exhibited prolonged intradiscal retention and superior therapeutic efficacy in vivo, as evidenced by improved MRI and disc-height parameters, preservation of NP architecture and proteoglycan-rich ECM, and reduced NLRP3/N-GSDMD-associated pyroptotic signaling, inflammation, and matrix catabolism. Together with their favorable systemic biocompatibility, these findings support Fm-IMH-CDs as a multifunctional platform capable of integrating biomimetic delivery, NLRP3 intervention, and redox regulation to attenuate IVDD progression.

Discussion

In this study, we established an integrated pathological framework linking NLRP3-associated pyroptosis, oxidative stress, and IVDD progression, and developed a functional reprogramming strategy for broader anti-pyroptotic intervention. Single-cell transcriptomic analysis and human tissue validation revealed state-dependent enrichment of pyroptosis-associated programs during NPC degeneration, with NLRP3 emerging as a prominent molecular feature. Phenotype-based screening of marine natural products identified IMH as an anti-pyroptotic compound, and subsequent target-validation studies established NLRP3 as its direct molecular target. However, the preferential activity of IMH against NLRP3-associated pyroptosis and its limited intrinsic antioxidant capacity highlighted the constraints of pathway-selective intervention. We therefore reprogrammed IMH into Ru-containing carbon dots that retained NLRP3 target engagement while acquiring multienzyme-mimetic ROS-regulatory activity, followed by platelet/NPC

hybrid membrane coating to enhance pathological-cell interaction and intradiscal retention. By integrating NLRP3 inhibition with ROS regulation, Fm-IMH-CDs broadened the anti-pyroptotic activity of IMH, alleviated oxidative and mitochondrial dysfunction, and remodeled disease-associated inflammatory networks. These effects ultimately translated into reduced pyroptosis, inflammation, and ECM degeneration and attenuated IVDD progression in vivo. Collectively, our findings demonstrate that functional reprogramming can transform a pathway-selective natural product into a multifunctional platform that simultaneously targets a key pyroptotic node and the oxidative microenvironment sustaining inflammatory injury.

Pyroptosis in IVDD should not be viewed as a uniform cell-death program driven exclusively by NLRP3 activation. The canonical NLRP3–Caspase-1–GSDMD pathway has been widely implicated in NPC pyroptosis and inflammatory amplification during disc degeneration[37–39]. However, emerging evidence suggests the involvement of additional inflammasome sensors. AIM2 has been associated with DNA damage responses in degenerative NPCs, while NAIP/NLRC4 activation has been reported to cooperate with NLRP3 in promoting NPC pyroptosis[40,41]. Importantly, these pathways operate within an oxidative microenvironment, where excessive ROS accumulation and mitochondrial dysfunction can amplify inflammasome activation and inflammatory injury[10,42]. Previous studies have demonstrated that ROS/TXNIP/NLRP3 signaling promotes NPC pyroptosis, whereas Nrf2-mediated suppression of TXNIP/NLRP3 signaling attenuates pyroptosis and ECM degradation[37,38]. Consistently, Mn-containing catalytic nanodots have been shown to alleviate experimental IVDD by scavenging ROS and suppressing pyroptosis[29]. Therefore, these observations suggest that effective anti-pyroptotic therapy may require not only blockade of a major inflammasome node, but also regulation of the oxidative environment that facilitates convergent inflammatory cell-death signaling.

Within this network, NLRP3 represents an attractive but incomplete therapeutic entry point. Pharmacological inhibition of NLRP3 has been shown to suppress NPC pyroptosis and attenuate experimental disc degeneration[20,43]. Natural bioactive molecules such as morin and honokiol have likewise been reported to ameliorate IVDD by suppressing TXNIP/NLRP3-associated inflammatory and pyroptotic signaling[44,45]. Our study extends these observations by identifying IMH through phenotype-based screening and subsequently establishing a direct structural and functional link between IMH and NLRP3. However, free IMH exhibited preferential activity under NLRP3-activating conditions and lacked appreciable intrinsic ROS-scavenging capacity. Thus, the limitation of IMH was not insufficient activity against its molecular target, but insufficient functional breadth to address the oxidative and signaling complexity of the degenerative microenvironment. Therefore, we do not simply regard IMH as a novel NLRP3 inhibitor, but further propose it as a functionally reprogramming precursor with a well-defined target basis.

To overcome this limitation, we employed carbon-dot-based reprogramming to expand the pharmacological scope of IMH while preserving its molecular basis. Precursor-derived carbon dots can retain biological features of active precursors while acquiring additional physicochemical and catalytic

properties during carbonization[46,47]. In our system, carbon-dot conversion preserved NLRP3 target engagement, whereas Ru incorporation conferred SOD-, CAT-, and GPx-like activities. Accordingly, Ru-containing IMH-CDs and Fm-IMH-CDs broadened the protective spectrum of free IMH from preferential NLRP3 inhibition to protection against poly(dA:dT)-, flagellin-, and Pam3CSK4-associated injury. This expanded protection was partially reversed by exogenous H_2O_2, supporting ROS regulation as a major contributor to the acquired broader activity. Rather than representing a distinct pyroptotic pathway, ROS regulation likely attenuates a shared oxidative pressure that facilitates multiple inflammatory and inflammasome-associated injury routes. Consistently, Fm-IMH-CDs reduced intracellular and mitochondrial ROS, restored mitochondrial function, and remodeled NOD-like receptor and NF-κB signaling. Together, these findings indicate that functional reprogramming expands a pathway-selective NLRP3 inhibitor toward broader anti-pyroptotic regulation by integrating direct target engagement with modulation of the oxidative and inflammatory microenvironment[48].

Beyond pharmacological reprogramming, hybrid membrane camouflage introduced a complementary delivery dimension. Platelet membranes provide inflammation-associated adhesion and homing properties[49,50], whereas NPC-derived membranes facilitate homotypic cellular interactions. The combination could enable the hybrid membrane to integrate inflammation-directed tropism with NPC-oriented recognition. Consistent with this design, Fm-IMH-CDs preferentially associated with pyroptotic NPCs, an effect attenuated by MCC950-mediated suppression of pyroptosis, and exhibited prolonged intradiscal retention in vivo. These properties translated into improved disc structure and ECM preservation, accompanied by reduced pyroptosis, inflammation, and matrix degradation in experimental IVDD. Thus, the therapeutic advantage of Fm-IMH-CDs arises from three complementary levels of intervention: NLRP3 targeting at the molecular level, ROS regulation at the pathological-microenvironment level, and biomimetic recognition and retention at the delivery level. Together, this architecture transforms a pathway-selective natural product into a multidimensional platform capable of regulating the interconnected pyroptosis–oxidative stress–inflammation–matrix degeneration network.

Several limitations should nevertheless be acknowledged. First, although single-cell transcriptomic and pseudotime analyses revealed state-dependent enrichment of pyroptosis-associated programs during NPC degeneration, pseudotime inference does not establish temporal causality or direct lineage relationships. Future studies integrating spatial transcriptomics, longitudinal human specimens, and lineage-resolved approaches will be required to determine whether pyroptosis actively drives early NPC-state transitions or accompanies their establishment. Second, although multiple approaches demonstrated direct IMH–NLRP3 interaction and identified M661 as an important contributor to the binding interface, the structural consequences of IMH binding on NLRP3 conformational activation, NEK7 interaction, oligomerization, and inflammasome assembly remain to be elucidated. Third, although Fm-IMH-CDs exhibited broader cytoprotection under AIM2-, NLRC4-, and noncanonical inflammasome-associated stimulation, these findings were primarily supported by cell-viability and ROS-rescue experiments. Further studies should directly examine pathway-specific inflammasome assembly, inflammatory caspase activation, and GSDMD cleavage to define how redox regulation influences

distinct pyroptotic routes. Fourth, therapeutic efficacy was primarily evaluated in a puncture-induced rat IVDD model. Although this model is reproducible and widely used for preclinical evaluation, it represents an acute injury-driven process and cannot fully recapitulate the chronic, heterogeneous, and multifactorial natural history of human IVDD[51,52]. Long-term and large-animal studies will therefore be necessary before clinical translation. Finally, further investigation is required to define the long-term biodistribution, degradation, Ru metabolism and clearance, immunogenicity and standardization of the hybrid membrane, batch-to-batch reproducibility, scale-up manufacturing, and quality control of Fm-IMH-CDs. These challenges remain broadly relevant to pharmacologically active carbon dots and cell-membrane-camouflaged nanomedicines[46,53].

Conclusion

In conclusion, this study establishes functional reprogramming as a strategy to expand pathway-selective NLRP3 inhibition toward broader anti-pyroptotic intervention in IVDD. We identified IMH as a marine-derived NLRP3-targeting compound and transformed it into Fm-IMH-CDs by integrating Ru-mediated carbon-dot engineering with platelet/NPC hybrid membrane camouflage. This reprogramming preserved NLRP3 target engagement while introducing multienzyme-mimetic ROS regulation and biomimetic recognition, thereby enabling coordinated modulation of pyroptosis, oxidative stress, inflammation, and ECM degeneration. Fm-IMH-CDs consequently exhibited broader cytoprotection and attenuated IVDD progression in vivo. Collectively, our findings provide a functional-reprogramming paradigm for converting a pathway-selective natural product into a multidimensional therapeutic platform and support broad-spectrum anti-pyroptosis as a potential strategy for IVDD treatment.

Methods

Single-cell RNA sequencing analysis and bioinformatics analysis

Human nucleus pulposus (NP) single-cell RNA sequencing (scRNA-seq) data were obtained from the Gene Expression Omnibus (GEO) database under accession number GSE165722. This dataset comprises eight human NP samples spanning different degrees of intervertebral disc degeneration (IVDD), including Pfirrmann grades II–V. The samples were categorized into normal (II), mildly degenerated (III), and severely degenerated (IV and V) groups according to the degeneration classification used in the present analysis. The original sequencing data were generated using the BD Rhapsody single-cell platform

Raw gene expression matrices were imported into R (version 4.5.3) and processed using the Seurat package (version 4.3.0). Low-quality cells were excluded according to the following criteria: fewer than 200 or more than 4,000 detected genes, and mitochondrial gene expression exceeding 20% of total transcript counts. Genes expressed in fewer than three cells were also removed. After quality control, the

remaining cells were normalized using the NormalizeData function with the LogNormalize method and a scale factor of 10,000. The top 2,000 highly variable genes were identified using FindVariableFeatures with the vst selection method. Data were subsequently centered and scaled using ScaleData, followed by principal component analysis (PCA) using RunPCA. The first 20 principal components were used for graph-based clustering and dimensionality reduction. Cell clusters were identified using FindNeighbors and FindClusters with a resolution of 0.5, and visualized using uniform manifold approximation and projection (UMAP).

Cell populations were annotated according to the expression of established lineage-specific markers. NPCs were identified by the expression of HAPLN1, ASPN, and CNMD; neutrophils by FCGR3B, CXCR1, and FPR1; macrophages by C1QA, C1QC, and FOLR2; T cells by CD3D, CD3G, and CD2; B cells by MS4A1, CD79A, and IGHM; erythroid cells by GYPA, SLC4A1, and ALAS2; and endothelial cells by EMCN, KDR, and CLEC14A. Seven major cell populations were identified. NPCs were subsequently extracted and subjected to independent normalization, dimensionality reduction, and reclustering. Based on their transcriptional signatures, NPCs were classified into six subpopulations: Met_NPCs, Effector_NPCs, Degenerative_NPCs, Adh_NPCs, Homeostatic_NPCs, and Fibro_NPCs.

Pyroptosis score of NP subclusters

To evaluate pyroptosis-associated transcriptional activity, a curated pyroptosis-related gene set was obtained from the Molecular Signatures Database (MSigDB; GOBP_PYROPTOTIC_INFLAMMATORY_RESPONSE, GO:0070269). Genes not detected in the scRNA-seq dataset were excluded before scoring. Pyroptosis scores were calculated for individual NPCs using the AddModuleScore function in Seurat (version 4.3.0), with 24 expression bins and 100 expression-matched control genes per feature. The resulting scores were compared across degeneration groups and NPC subpopulations and further integrated with pseudotime analysis to characterize changes in pyroptosis-associated transcriptional activity during NPC-state transitions.

Pseudotime trajectory analysis

To investigate transcriptional state transitions during nucleus pulposus cell (NPC) degeneration, pseudotime trajectory analysis was performed using Monocle 2 (version 2.18.0). The NPC expression matrix and corresponding cell annotations obtained from Seurat were used to construct a CellDataSet object. Size factors and dispersion parameters were estimated using the estimateSizeFactors and estimateDispersions functions, respectively. Genes exhibiting significant differential expression among NPC subpopulations were identified using the differentialGeneTest function, with a false discovery rate (FDR)-adjusted P value (q value) < 0.01. These genes were selected as ordering genes using setOrderingFilter. Dimensionality reduction was performed using the discriminative dimensionality reduction with trees (DDRTree) algorithm, with max_components = 2. Cells were subsequently ordered along the reconstructed trajectory using the orderCells function, and pseudotime values were assigned

to individual NPCs. The resulting trajectories were visualized according to NPC subpopulations, degeneration groups, and pseudotime. Changes in pyroptosis scores and the expression of representative pyroptosis-associated genes were examined along the inferred trajectories to characterize their relationships with NPC-state remodeling.

In parallel, cellular differentiation potential was estimated using the CytoTRACE R package (version 0.3.3). The NPC gene expression matrix was analyzed using the cytoTRACE function with default parameters. CytoTRACE scores, ranging from 0 to 1, were assigned to individual cells, with higher scores indicating greater predicted differentiation potential and lower scores indicating more differentiated transcriptional states. CytoTRACE scores were subsequently integrated with NPC subpopulation annotations and pseudotime trajectories to investigate the relationship between cellular differentiation potential and degeneration-associated transcriptional remodeling. Associations between pyroptosis scores and pseudotime values were assessed using Spearman's rank correlation analysis. Statistical significance was defined as a two-sided $P < 0.05$.

Human intervertebral disc tissue collection and analysis

Human intervertebral disc tissues were obtained from patients undergoing spinal surgery. Samples were classified according to the Pfirrmann grading system and divided into mildly degenerated (grade II) and severely degenerated (grades IV–V) groups. Written informed consent was obtained from all participants. Tissues were fixed in 4% paraformaldehyde for 24 h, dehydrated through graded ethanol, embedded in paraffin, and sectioned at a thickness of 5 μm. Following deparaffinization and rehydration, sections were subjected to heat-induced antigen retrieval in Tris-EDTA buffer (pH 9.0), followed by blocking of endogenous peroxidase activity and nonspecific antibody binding. Sections were incubated overnight at 4°C with primary antibodies against MMP3 (66338-1-Ig, Proteintech; 1:500), NLRP3 (68102-1-Ig, Proteintech; 1:200), cleaved Caspase-1 (AF4005, Affinity Biosciences; 1:100), GSDMD (AF4012, Affinity Biosciences; 1:100), and IL-1β (16806-1-AP, Proteintech; 1:200).

Isolation and culture of primary cells and differentiation of bone marrow-derived macrophages

Primary rat NPCs

Rat NPCs were isolated from the intervertebral discs of Sprague-Dawley rats[54]. Briefly, nucleus pulposus tissues were aseptically harvested under a stereomicroscope, carefully separated from the surrounding annulus fibrosus and cartilaginous endplates, and washed three times with sterile phosphate-buffered saline (PBS). The isolated tissues were minced into approximately 1 mm^3 fragments and digested with 0.2% type II collagenase at 37°C for 4 h. Following digestion, the cell suspension was filtered through a 70 μm cell strainer and centrifuged at 300 × g for 5 min. The collected cells were resuspended in Dulbecco's modified Eagle's medium/Ham's F-12 (DMEM/F12; Gibco) supplemented with 10% fetal

bovine serum (FBS; Gibco) and 1% penicillin–streptomycin. Cells were maintained at 37°C in a humidified atmosphere containing 5% CO_2, and the culture medium was replaced every 2–3 days. Cells at passages 2–3 were used for subsequent experiments.

Primary rat endplate chondrocytes (EPCs)

EPCs were isolated from the cartilaginous endplates of Sprague-Dawley rats[55]. After aseptic dissection of the intervertebral discs, the nucleus pulposus and annulus fibrosus tissues were carefully removed to expose the cartilaginous endplates. The endplate cartilage was collected under a stereomicroscope, washed with sterile PBS, and minced into approximately 1 mm^3 fragments. Tissue fragments were digested with 0.2% type II collagenase at 37°C for 4 h. The resulting cell suspension was filtered through a 70 μm cell strainer and centrifuged at 300 × g for 5 min. Isolated EPCs were cultured in DMEM/F12 supplemented with 10% FBS and 1% penicillin–streptomycin at 37°C under 5% CO_2. The culture medium was replaced every 2–3 days, and cells at passages 1–3 were used for subsequent experiments.

Mouse bone marrow-derived macrophages (BMDMs)

BMDMs were generated from the femurs and tibias of C57BL/6J mice. [56] Briefly, bone marrow cells were flushed from the medullary cavities using sterile PBS, filtered through a 70 μm cell strainer, and collected by centrifugation at 300 × g for 5 min. The resulting cells were resuspended in DMEM supplemented with 10% FBS, 1% penicillin–streptomycin, and 50 ng/mL recombinant mouse macrophage colony-stimulating factor (M-CSF). Cells were cultured at 37°C under 5% CO_2 for 7 days to induce macrophage differentiation. Fresh M-CSF-containing medium was replenished during differentiation. On day 7, adherent macrophages were collected and used for subsequent inflammasome activation experiments.

Mouse bone marrow-derived mesenchymal stem cells (BMSCs)

BMSCs were isolated from the femurs and tibias of C57BL/6J mice [57]. Briefly, the long bones were aseptically collected, and the surrounding muscle and connective tissues were removed. After excision of the epiphyses, bone marrow was flushed from the medullary cavities using sterile PBS. The collected marrow suspension was passed through a 70 μm cell strainer and centrifuged at 300 × g for 5 min. The resulting cells were resuspended in α-minimum essential medium (α-MEM; Gibco) supplemented with 15% FBS and 1% penicillin–streptomycin and seeded into culture flasks. Cells were maintained at 37°C in a humidified atmosphere containing 5% CO_2. After initial attachment, nonadherent hematopoietic cells were removed by replacing the culture medium. Adherent cells were subsequently expanded, with medium replacement every 2–3 days. Cells were passaged upon reaching approximately 80–90% confluence, and passages 3–5 were used for subsequent experiments.

Induction of NLRP3-associated pyroptosis and compound screening

For classical NLRP3 inflammasome activation, NPCs were primed with lipopolysaccharide (LPS, 1 μg/mL) for 3 h, followed by stimulation with ATP (5 mM) for 1 h to induce inflammasome assembly and pyroptotic cell death. During ATP stimulation, cells were treated with Marine Natural Product Library (L6400, https://www.targetmol.cn/compound-library/marine_natural_product_library) for another 3 hours. Then, cell viability assay (CCK8) was performed to screen potential pyroptosis inhibitors. For the second round of screening experiments, NPCs were seeded into 96-well plates and allowed to adhere overnight. Pyroptotic injury was subsequently induced using the established model conditions. Candidate compounds identified from the primary screening were evaluated over a concentration range of 0.1, 0.5, 1, 2, 5, 10, 20, and 30 μM. NPCs were treated with the indicated concentrations of each candidate compound, while untreated cells and pyroptosis-induced cells without compound treatment served as the control and model groups, respectively. After treatment, cell viability was determined using a CCK-8 assay. The concentration-dependent cytoprotective effects of the candidate compounds were compared to identify the lead compound for subsequent mechanistic studies. MCC950 was additionally included as a reference NLRP3 inhibitor during the screening process. Based on the screening results, 5-[(1H-indol-3-yl)methylidene]imidazolidine-2,4-dione (IMH) was selected for subsequent mechanistic and therapeutic investigations.

LPS/ATP-induced cell injury and treatment

To evaluate the protective effects of the indicated treatment against LPS/ATP-induced inflammatory cell injury, primary rat NPCs, rat EPCs, mouse BMSCs, and mouse BMDMs were subjected to the same stimulation protocol. Cells were first primed with lipopolysaccharide (LPS) for 3 h, followed by stimulation with ATP for 1 h to induce inflammatory cell injury. IMH was added simultaneously with LPS and maintained in the culture medium for 3 h at final concentrations of 1, 2, or 5 μM. Untreated cells served as the control group, whereas cells exposed to LPS/ATP without therapeutic treatment served as the model group. Following treatment, cell viability was assessed using a CCK-8 assay, and plasma membrane damage was evaluated by measuring lactate dehydrogenase (LDH) release into the culture supernatant. Cell viability was normalized to the untreated control group, and LDH release was expressed relative to the control group.

Induction of pathway-specific inflammasome activation and treatment

For pathway-specific inflammasome activation assays, distinct inflammasome stimuli were applied. AIM2 inflammasome activation was induced by transfection with poly(dA:dT) (500 ng/mL, HY-138646, MedChemExpress), whereas NLRC4 inflammasome activation was induced by transfection with flagellin (250 ng/mL; tlrl-stfla, InvivoGen). For noncanonical inflammasome activation, cells were primed with Pam3CSK4 (400 ng/mL; HY-P1180, MedChemExpress), followed by intracellular delivery of LPS (LPS; HY-D1056, MedChemExpress) using a transfection reagent according to the manufacturer's instructions.

Cell viability and cytotoxicity were subsequently assessed to determine the protective efficacy of IMH against stimulus-induced cell injury.

Cell viability and cytotoxicity assessment

Cell viability was evaluated using the Cell Counting Kit-8 (CCK-8; HY-K0301, MedChemExpress, USA) according to the manufacturer's protocol. Briefly, cells were incubated with CCK-8 reagent for the indicated duration, and absorbance was measured at 450 nm using a microplate reader.

Cell membrane damage was assessed by measuring lactate dehydrogenase(LDH; HY-K1090, MedChemExpress, USA) release in culture supernatants. The percentage of LDH release was calculated according to the manufacturer's instructions.

Flow cytometric analysis of pyroptosis

Pyroptotic cell death was assessed using a FAM-FLICA Caspase-1 Assay Kit (ICT-97, ImmunoChemistry Technologies, USA) combined with propidium iodide (PI) staining. Following the indicated treatments, cells were harvested and incubated with the FAM-YVAD-FMK fluorescent probe according to the manufacturer's instructions. After washing to remove unbound probe, cells were stained with PI and immediately analyzed by flow cytometry. Cells positive for both activated caspase-1 and PI were quantified as the percentage of FAM-FLICA^{+}/PI^{+} cells to evaluate pyroptosis-associated cell death.

Molecular docking for potential cell-death regulatory targets

Molecular docking was performed to screen potential pyroptosis-related protein targets of IMH. Eight proteins involved in inflammasome activation and pyroptotic cell death, including AIM2, caspase-1 (CASP1), gasdermin D (GSDMD), NEK7, NINJ1, NLRC4, NLRP3, and Pyrin (MEFV), were selected as candidate targets. Target protein crystal structures were retrieved from the PDB database (http://www.rcsb.org/). Three-dimensional protein structures were obtained from the Protein Data Bank (PDB) or the AlphaFold Protein Structure Database when experimentally resolved structures were unavailable. Protein structures were prepared using PyMOL (version 2.3.0) by removing water molecules, co-crystallized ligands, and other nonessential components. The three-dimensional structure of IMH was subjected to energy minimization using Chem3D (2020). The prepared proteins and IMH were converted to PDBQT format using AutoDockTools (version 1.5.6). Molecular docking was subsequently performed using AutoDock Vina (version 1.2.0) with a semi-flexible docking protocol, an exhaustiveness value of 16, and a maximum of nine output poses for each protein–ligand pair. Candidate targets were ranked according to their predicted binding energies, with more negative binding energies indicating more

favorable predicted interactions. The optimal docking poses were selected for interaction analysis and visualized using PyMOL (version 2.3.0).

Molecular dynamics simulation

Molecular dynamics (MD) simulations were performed to evaluate the dynamic stability of the NLRP3-IMH complex. The protein was parameterized using the CHARMM36 all-atom force field, while ligand parameters were generated using the CHARMM General Force Field (CGenFF). The complex was placed in a dodecahedral simulation box with a minimum distance of 1.0 nm from the box boundary, solvated with the TIP3P water model, and neutralized by adding Na^+ or Cl^- counterions. Energy minimization was performed using the steepest-descent algorithm until the maximum force was below 1,000 $kJ \cdot mol^{-1} \cdot nm^{-1}$. The system was subsequently equilibrated for 100 ps under the NVT ensemble at 300 K using the V-rescale thermostat, followed by 100 ps under the NPT ensemble at 1 bar using the Parrinello–Rahman barostat. A 100 ns production MD simulation was then performed with a 2 fs time step. All covalent bonds were constrained using the LINCS algorithm, and long-range electrostatic interactions were calculated using the particle mesh Ewald (PME) method with a cutoff of 1.2 nm. Trajectories were saved every 10 ps and analyzed for root-mean-square deviation (RMSD), root-mean-square fluctuation (RMSF), radius of gyration (Rg), solvent-accessible surface area (SASA), and protein–ligand hydrogen bonds. Principal component analysis (PCA) and Gibbs free-energy landscape (FEL) analysis were further performed to characterize the conformational dynamics and energetically favorable states of the complex. Binding free energy and per-residue energy contributions were calculated from representative equilibrated trajectories using the MM/PBSA method implemented in gmx_MMPBSA.

Surface plasmon resonance (SPR) assay

Surface plasmon resonance (SPR) analysis was performed using a Biacore 8K system equipped with a CM5 sensor chip (Cytiva) to determine the binding affinity between IMH and NLRP3. The sensor surface was activated with 400 mM EDC and 100 mM NHS, and recombinant NLRP3 protein (20 μg/mL) was immobilized onto the sample flow cell (Fc2) by amine coupling to an immobilization level of approximately 12,600 response units (RU), while Fc1 served as the reference channel. IMH was serially diluted to concentrations ranging from 1.56 to 100 μM and injected over both flow cells at a flow rate of 20 μL/min, with an association time of 60 s followed by a dissociation time of 90 s. The sensor surface was regenerated after each cycle. Sensorgrams were reference-subtracted and fitted using a 1:1 Langmuir binding model with Biacore Insight Evaluation Software (Cytiva) to determine the association rate constant (k□), dissociation rate constant (k_d), and equilibrium dissociation constant (K_D).

Drug Affinity Responsive Target Stability (DARTS)

DARTS assays were performed to evaluate the direct interaction between IMH and NLRP3 based on ligand-induced resistance to proteolysis. For endogenous NLRP3 analysis, cell lysates were incubated with IMH at the indicated concentrations (5, 50, or 500 μM) or an equivalent volume of DMSO, followed by limited proteolysis with Pronase. Proteolysis was terminated by the addition of protease inhibitors, and the remaining NLRP3 protein was analyzed by Western blotting, with β-actin used as the loading control. To further assess direct target engagement, recombinant NLRP3 protein was incubated with IMH under the same conditions before Pronase digestion, and the residual NLRP3 protein was quantified by immunoblotting. For binding-site validation, cells expressing Flag-tagged wild-type (WT) or mutant NLRP3 constructs (including M661A, Y632A, and I411A) were treated with IMH and subjected to the same DARTS procedure. Protein band intensities were quantified by densitometric analysis and normalized to the corresponding undigested controls. Increased resistance of NLRP3 to Pronase-mediated degradation in the presence of IMH was interpreted as evidence of IMH-induced stabilization of NLRP3.

Cellular Thermal Shift Assay (CETSA)

CETSA assays were performed to evaluate the interaction between IMH and NLRP3 based on ligand-induced changes in protein thermal stability. For endogenous NLRP3 analysis, cells were treated with IMH or an equivalent volume of DMSO and subsequently harvested and resuspended in PBS supplemented with protease inhibitors. Equal aliquots of the cell suspension were heated at the indicated temperatures (37, 43, 48, 53, 58, 63, 69, and 73°C), followed by cooling and cell lysis. Insoluble heat-denatured proteins were removed by centrifugation, and the soluble fractions were collected for Western blot analysis of NLRP3. For the recombinant-protein thermal stability assay, recombinant NLRP3 was incubated with IMH or DMSO and subjected to a temperature gradient (37, 45, 57, 66, and 73°C), after which the remaining soluble NLRP3 was analyzed by immunoblotting. To further evaluate the contribution of the predicted binding residue, Flag-tagged NLRP3-M578A was subjected to the same thermal stability assay. Protein band intensities were quantified by densitometry, normalized to the corresponding unheated or lowest-temperature control, and plotted against temperature to generate thermal stability curves. An IMH-induced shift in the thermal stability of NLRP3 was considered supportive of target engagement.

Preparation of platelet–NPC hybrid membranes (Fm)

Platelet-NPC hybrid membranes were prepared by membrane isolation followed by membrane fusion. Briefly, platelets were collected and washed with ice-cold PBS, followed by repeated centrifugation to remove residual plasma components. Platelet membranes were obtained by repeated freeze-thaw cycles and centrifugation, and the resulting membrane fraction was resuspended in PBS. For preparation of NPC membranes, cultured NPCs were harvested, washed with ice-cold PBS, and lysed in hypotonic lysis buffer supplemented with protease inhibitors. The cell suspension was mechanically disrupted and

subjected to differential centrifugation to remove intact cells, nuclei, and intracellular debris, followed by high-speed centrifugation to collect the plasma membrane fraction. The isolated platelet membranes and NPC membranes were mixed at a protein mass ratio of 1:1 and fused using a liposome extruder. The membrane mixture was sequentially extruded through 400- and 200-nm polycarbonate membranes for 10 passes each to facilitate membrane fusion and generate platelet–NPC hybrid membrane vesicles (Fm). The resulting hybrid membranes were collected and stored at 4°C for immediate use. The morphology and membrane architecture of the platelet–NPC hybrid membranes and Fm-IMH-CDs were characterized by cryogenic transmission electron microscopy (cryo-TEM). The retention of platelet-specific CD41 and NPC-associated CD24 was evaluated by Western blotting using anti-CD41 (R22855, Zenbio, China) and anti-CD24 (R30109, Zenbio, China) antibodies, respectively. GAPDH was also examined to assess the presence of intracellular protein contamination.

Synthesis of IMH-CDs and Fm-IMH-CDs

IMH and $RuCl_3$ were dissolved in ultrapure water and heated in a Teflon-lined autoclave at 180°C for 8 h. After cooling, the dispersion was dialyzed against ultrapure water to obtain IMH-CDs. Ru-free IMH-CDs were prepared without $RuCl_3$. Membrane protein concentrations were determined by the BCA assay. Hybrid membranes were combined with IMH-CDs at a carbon-dot-to-membrane-protein mass ratio of 2:1 and bath-sonicated for 2 min to prepare Fm-IMH-CDs.

Characterization

Morphology was examined by TEM and high-resolution TEM using a JEM-2100F microscope (JEOL, Japan; 200 kV). Hydrodynamic size and zeta potential were measured using a ZEN 3600 Zetasizer (Malvern Instruments, UK). Hybrid membranes and Fm-IMH-CDs were examined by cryo-TEM after plunge-freezing in liquid ethane. XRD patterns were acquired using a D/MAX-2200 PC diffractometer (Rigaku, Japan; Cu Kα radiation). XPS survey and high-resolution C 1s, Ru 3p, and O 1s spectra were recorded using an ESCALAB 250 spectrometer (Thermo Fisher Scientific, USA), with binding energies referenced to C-C at 284.8 eV. Equal membrane-protein amounts were analyzed by SDS-PAGE and Coomassie brilliant blue staining. Western blotting was performed using antibodies against mouse CD41, CD24, and GAPDH, followed by HRP-conjugated secondary antibodies and chemiluminescence detection. GAPDH was assessed as a marker of cytoplasmic contamination.

Enzyme-mimetic activities

Total antioxidant capacity was measured by ABTS radical-cation decolorization. ABTS was reacted with potassium persulfate for 12 h in the dark, and the working solution was adjusted to an absorbance of approximately 0.70 at 734 nm. After incubation with material for 10 min, absorbance was measured at

734 nm. Results were calculated using a Trolox calibration curve and expressed as Trolox-equivalent antioxidant capacity. A concentration series was used for the dose-response analysis.

SOD-like activity was assessed using the xanthine/xanthine oxidase-WST-1 assay. Formazan formation was monitored at 450 nm according to the assay kit instructions. Inhibition was calculated as 100 × (1 - A□/A□), where A_S and A_C represent background-corrected sample and control absorbances.

CAT-like activity was evaluated by monitoring the decrease in absorbance of 10 mM H_2O_2 at 240 nm. H_2O_2 decomposition was calculated as 100 × (C□ − C□)/C□, using residual substrate concentrations in the control and sample at the same reaction time.

GPx-like activity was measured using a glutathione reductase-coupled assay containing 8.4 mM GSH, 300 μM NADPH, and glutathione reductase supplied with the Beyotime assay kit. Reactions were initiated with 5 mM H_2O_2. Activity was evaluated from the background-corrected initial rate of NADPH absorbance decrease at 340 nm.

Computational analysis

Density functional theory calculations compared oxygen-functionalized carbon frameworks with and without a supported Ru cluster. Adsorbed intermediates in the GPx-like, SOD-like, and CAT-like pathways were examined, with CH_3SH serving as a simplified thiol model for the GPx-like pathway. Relative energies were referenced to stoichiometrically balanced initial states. Intermediate energy differences were distinguished from activation barriers.

Preferential targeting of pyroptotic NPCs and heterotypic cellular uptake assay

The preferential targeting of hybrid membrane-coated nanoparticles toward pyroptotic NPCs and their cellular selectivity were evaluated by fluorescence imaging. FITC-labeled IMH-CDs were coated with either NPC membrane (m-IMH-CDs) or platelet–NPC hybrid membrane (Fm-IMH-CDs). Normal NPCs and pyroptotic NPCs were incubated with equivalent concentrations of m-IMH-CDs or Fm-IMH-CDs for the indicated period. To determine whether the preferential association of Fm-IMH-CDs was dependent on the pyroptotic cell state, pyroptotic NPCs were pretreated with the NLRP3 inhibitor MCC950 before incubation with Fm-IMH-CDs. Bone marrow-derived macrophages (BMDMs) were used as heterotypic control cells and exposed to m-IMH-CDs or Fm-IMH-CDs under identical conditions to evaluate nonspecific cellular association. Following incubation, cells were thoroughly washed with PBS to remove unbound nanoparticles, fixed with 4% paraformaldehyde, and counterstained with DAPI. Nanoparticle-associated FITC fluorescence was visualized by confocal laser scanning microscopy (CLSM), and the fluorescence intensity was quantified to compare cellular association among the different groups.

Lysosomal colocalization assay

Lysosomal colocalization assay was performed to investigate the intracellular trafficking of IMH-CDs and Fm-IMH-CDs. NPCs were incubated with FITC-labeled IMH-CDs or Fm-IMH-CDs for the indicated period and subsequently stained with LysoTracker™ Red DND-99 (L7528, Invitrogen, Thermo Fisher Scientific, USA) to visualize lysosomes. After washing with PBS, the cells were fixed with 4% paraformaldehyde and counterstained with DAPI to visualize nuclei. Fluorescence images were acquired using confocal laser scanning microscopy (CLSM). The spatial distribution of nanoparticles and lysosomes was further evaluated by fluorescence intensity line-profile analysis to assess their intracellular colocalization.

Cellular uptake mechanism assay

The cellular uptake mechanism of Fm-IMH-CDs was investigated using pharmacological inhibitors of major endocytic pathways and a low-temperature condition. NPCs were pretreated with chlorpromazine (HY-12708, MedChemExpress, USA), filipin III (HY-N6718, MedChemExpress, USA), or dynasore (HY-15304, MedChemExpress, USA) for the indicated period to inhibit clathrin-mediated endocytosis, cholesterol-dependent caveolae/lipid raft-mediated endocytosis, or dynamin-dependent endocytosis, respectively. For energy-dependence analysis, cells were incubated at 4°C to suppress energy-dependent cellular uptake. Following pretreatment, NPCs were exposed to FITC-labeled Fm-IMH-CDs in the continued presence of the corresponding inhibitor or under the 4°C condition. Cells maintained under standard culture conditions without inhibitor treatment served as the control. After incubation, the cells were thoroughly washed with PBS to remove extracellular nanoparticles, and nanoparticle-associated fluorescence was measured. FITC fluorescence intensity was normalized to that of the control group to evaluate the contribution of different uptake pathways.

Scanning electron microscopy (SEM)

Pyroptosis-associated morphological changes in NPCs were evaluated by scanning electron microscopy (SEM). NPCs were seeded onto sterile coverslips and subjected to the indicated treatments. After treatment, cells were gently washed with PBS and fixed with 2.5% glutaraldehyde at 4°C overnight. The samples were then washed with PBS, dehydrated through a graded ethanol series, subjected to critical-point drying, mounted onto SEM stubs, and sputter-coated with gold. The ultrastructural morphology of the NPC plasma membrane was subsequently examined using a scanning electron microscope, with particular attention to pyroptosis-associated morphological alterations, including cell swelling, membrane blebbing, and loss of plasma membrane integrity.

Intracellular ROS detection

Intracellular ROS levels were assessed using a DCFH-DA-based Reactive Oxygen Species Assay Kit (S0033S, Beyotime Biotechnology, China). Following the indicated treatments, NPCs were washed with PBS and incubated with DCFH-DA in serum-free medium according to the manufacturer's instructions. After incubation at 37°C in the dark, cells were washed thoroughly to remove excess probe and immediately imaged using a fluorescence microscope. Intracellular ROS production was quantified based on the mean fluorescence intensity of DCF.

Mitochondrial membrane potential assay

Mitochondrial membrane potential (ΔΨm) was assessed using a JC-1 Mitochondrial Membrane Potential Assay Kit (C2006, Beyotime Biotechnology, China) according to the manufacturer's instructions. Following the indicated treatments, NPCs were incubated with JC-1 staining solution at 37°C in the dark according to the manufacturer's protocol. Cells were subsequently washed with JC-1 staining buffer and examined by fluorescence microscopy. JC-1 aggregates exhibiting red fluorescence indicate relatively preserved mitochondrial membrane potential, whereas JC-1 monomers exhibiting green fluorescence indicate mitochondrial depolarization. Mitochondrial membrane potential was evaluated by calculating the fluorescence intensity ratio of JC-1 aggregates to monomers.

Mitochondrial ROS detection

Mitochondrial ROS production was assessed using MitoSOX™ Red Mitochondrial Superoxide Indicator (M36008, Invitrogen, Thermo Fisher Scientific, USA). After the indicated treatments, NPCs were washed with PBS and incubated with MitoSOX™ Red working solution at 37°C in the dark. After incubation, excess probe was removed by washing, and nuclei were counterstained with DAPI. Fluorescence images were acquired using a fluorescence or confocal microscope under identical imaging settings among groups. Mitochondrial superoxide production was quantified based on the mean MitoSOX fluorescence intensity and normalized to that of the control group.

RNA sequencing and bioinformatics analysis

Transcriptomic sequencing and bioinformatics analyses were performed by Gene-Kinder (Shanghai, China). Briefly, NPCs were divided into three groups: untreated control (Control), LPS/ATP-induced pyroptosis (IVDD), and Fm-IMH-CD-treated pyroptotic NPCs (Treatment). Total RNA was extracted from each group, and RNA quality and integrity were assessed before library preparation. Following library construction, high-throughput RNA sequencing was performed to characterize genome-wide transcriptional alterations. After quality control, sequencing reads were aligned to the corresponding reference genome, and gene expression levels were quantified. Principal component analysis (PCA) was conducted to assess the overall transcriptional differences among groups. Differentially expressed genes (DEGs) were identified through pairwise comparisons between the IVDD and Control groups and

between the Treatment and IVDD groups. Gene Ontology (GO) enrichment analysis was performed to characterize the biological processes (BP), cellular components (CC), and molecular functions (MF) associated with DEGs. Kyoto Encyclopedia of Genes and Genomes (KEGG) pathway enrichment analysis was conducted to identify signaling pathways potentially involved in pyroptosis and inflammatory regulation. Furthermore, gene set enrichment analysis (GSEA) was performed to evaluate coordinated transcriptional changes in predefined gene sets, with particular attention to the NOD-like receptor and NF-κB signaling pathways. Enrichment results were visualized using bar plots, bubble plots, and enrichment curves.

Establishment and treatment of the rat IVDD model

All animal experiments were performed in accordance with institutional guidelines for the care and use of laboratory animals and were approved by the Institutional Animal Care and Use Committee of our hospital (approval number: 2025034-A1). Male Sprague-Dawley rats (approximately 200 g) were randomly assigned to the Sham, IVDD, IMH-CDs, Fm-IMH-CDs, and other indicated control groups. Rats were anesthetized with isoflurane, and puncture-induced IVDD was established in the caudal intervertebral discs using a sterile needle. The needle was inserted into the nucleus pulposus through the annulus fibrosus to a controlled depth, rotated, and maintained in position for 30 s to induce reproducible disc injury. Sham-operated rats underwent the same procedure without disc puncture. Seven days after puncture, therapeutic intervention was initiated by local intradiscal injection. IMH-CDs or Fm-IMH-CDs were administered at a concentration of 20 μg/mL in an injection volume of 5 μL per disc (equivalent to 0.1 μg nanoparticles per disc), while the corresponding vehicle was administered to the indicated control groups. At 8 weeks after treatment, the rats were euthanized, and the intervertebral discs were harvested for imaging, histological, immunohistochemical, and molecular analyses.

Magnetic resonance imaging analysis

Magnetic resonance imaging (MRI) was performed to evaluate the progression of IVDD and the therapeutic efficacy of different treatments, with technical support provided by United Imaging Healthcare (Shanghai, China). At the designated time point, rats were anesthetized and positioned for MRI examination of the caudal intervertebral discs. T2-weighted images were acquired using an MRI system under identical imaging parameters for all experimental groups. Disc degeneration was evaluated based on alterations in nucleus pulposus T2 signal intensity and overall intervertebral disc morphology. The severity of IVDD was further assessed using the Pfirrmann grading system by investigators blinded to the experimental groups.

Histological staining and evaluation

Harvested intervertebral disc tissues were fixed in 4% paraformaldehyde, decalcified, dehydrated through graded ethanol solutions, embedded in paraffin, and sectioned into 5 μm slices. Hematoxylin and eosin

(H&E) staining was performed to evaluate overall tissue morphology, including nucleus pulposus structure, annulus fibrosus integrity, and cellular distribution. Safranin O/Fast Green staining was conducted to assess proteoglycan content and extracellular matrix degradation within the nucleus pulposus region. Histological changes were scored according to established IVDD grading criteria by two independent observers blinded to treatment groups.

Immunohistochemistry staining

Paraffin-embedded intervertebral disc sections were subjected to immunohistochemical (IHC) staining to evaluate the expression of proteins associated with extracellular matrix degradation, pyroptosis, and inflammation. Briefly, tissue sections were deparaffinized in xylene, rehydrated through a graded ethanol series, and subjected to heat-induced antigen retrieval. Following the inhibition of endogenous peroxidase activity and blocking of nonspecific binding, sections were incubated overnight at 4°C with primary antibodies against MMP3 (66338-1-Ig, Proteintech, China), NLRP3 (DF7438, Affinity Biosciences, China), cleaved-Caspase-1 (AF4005, Affinity Biosciences, China), GSDMD (AF4012, Affinity Biosciences, China), and IL-1β (AF5103, Affinity Biosciences, China). Subsequently, the sections were incubated with appropriate horseradish peroxidase (HRP)-conjugated secondary antibodies, followed by visualization using 3,3'-diaminobenzidine (DAB). Nuclei were counterstained with hematoxylin, and the sections were dehydrated, cleared, and mounted. Representative images were acquired using a light microscope under identical imaging conditions. The percentages of positively stained cells and the corresponding staining intensities were quantified using ImageJ software by investigators blinded to the experimental groups.

In vivo biodistribution analysis of nanoparticles

To evaluate the retention and distribution of nanoparticles within intervertebral discs, fluorescently labeled formulations were locally administered into the disc tissues. Fluorescence signals were monitored at different time points using an in vivo imaging system. The relative fluorescence intensity within the intervertebral disc region was quantified to compare the local retention ability of different formulations.

Statistical analysis

All statistical analyses were performed using GraphPad Prism (GraphPad Software, San Diego, CA, USA). Quantitative data are presented as the mean ± standard deviation (SD) unless otherwise indicated. The number of independent biological replicates (n) is specified in the corresponding figure legends. Data distribution was assessed for normality. Comparisons between two independent groups were performed using an unpaired two-tailed Student’s t-test when the assumptions of normality and equal variance were satisfied. For comparisons involving three or more groups with a single independent variable, one-way analysis of variance (ANOVA) followed by Tukey’s multiple-comparisons test was used. For datasets that

did not satisfy the assumptions required for parametric analyses, appropriate nonparametric tests were applied. Ordinal data, including Pfirrmann grades and histological scores, were analyzed using nonparametric statistical methods. A P value < 0.05 was considered statistically significant.

Declarations

Author Contribution

W.Li. designed the experiments and performed the major experimental work. L.H. conducted statistical analyses, interpreted the data, and drafted the original manuscript. W.Lin. and T.Y. performed experiments and contributed to data collection and validation. R.Z. participated in experimental procedures, data analysis, and verification of experimental results. X.L. and J.L. contributed to the study design, supervised experimental activities, and critically reviewed and revised the manuscript. H.Y. contributed to the study design, secured funding, supervised the overall research project, and critically reviewed and revised the manuscript. All authors read and approved the final manuscript.

Acknowledgement

We acknowledge the Central Laboratory, College of Basic Medical Sciences, Naval Medical University, for assistance with confocal imaging.

References

1. Hammoor BT, Lai CS, Xiong GX, et al. Intervertebral disc degeneration. Nat Rev Dis Primers Feb. 2026;5(1):5. 10.1038/s41572-025-00681-8.
2. Galbusera F, van Rijsbergen M, Ito K, Huyghe JM, Brayda-Bruno M, Wilke HJ. Ageing and degenerative changes of the intervertebral disc and their impact on spinal flexibility. Eur Spine J Jun. 2014;23(Suppl 3):S324–32. 10.1007/s00586-014-3203-4.
3. Eisenstein SM, Balain B, Roberts S. Current Treatment Options for Intervertebral Disc Pathologies. Cartilage Apr. 2020;11(2):143–51. 10.1177/1947603520907665.
4. Samanta A, Lufkin T, Kraus P. Intervertebral disc degeneration-Current therapeutic options and challenges. Front Public Health. 2023;11:1156749. 10.3389/fpubh.2023.1156749.
5. Luo Z, Wei Z, Zhang G, Chen H, Li L, Kang X. Achilles' Heel—The Significance of Maintaining Microenvironmental Homeostasis in the Nucleus Pulposus for Intervertebral Discs. Int J Mol Sci. 2023;24(23):16592.
6. Swahn H, Mertens J, Olmer M, et al. Shared and Compartment-Specific Processes in Nucleus Pulposus and Annulus Fibrosus During Intervertebral Disc Degeneration. Adv Sci (Weinh) May. 2024;11(17):e2309032. 10.1002/advs.202309032.

7. Jia S, Liu H, Yang T et al. Single-cell sequencing reveals cellular heterogeneity of nucleus pulposus in intervertebral disc degeneration. *Scientific Reports*. 2024/11/08 2024;14(1):27245. 10.1038/s41598-024-78675-x
8. Vande Walle L, Lamkanfi M. Drugging the NLRP3 inflammasome: from signalling mechanisms to therapeutic targets. *Nature Reviews Drug Discovery*. 2024/01/01 2024;23(1):43–66. 10.1038/s41573-023-00822-2
9. Chao-yang G, Peng C, Hai-hong Z. Roles of NLRP3 inflammasome in intervertebral disc degeneration. *Osteoarthritis and Cartilage*. 2021/ 06/01 / 2021;29(6):793–801. doi:https://doi.org/10.1016/j.joca.2021.02.204.
10. Zhou R, Yazdi AS, Menu P, Tschopp J. A role for mitochondria in NLRP3 inflammasome activation. Nature 2011/01/01. 2011;469(7329):221–5. 10.1038/nature09663.
11. Xu Q, Xing H, Wu J, Chen W, Zhang N. miRNA-141 Induced Pyroptosis in Intervertebral Disk Degeneration by Targeting ROS Generation and Activating TXNIP/NLRP3 Signaling in Nucleus Pulpous Cells. Front Cell Dev Biol. 2020;8:871. 10.3389/fcell.2020.00871.
12. Chen X, Zhang A, Zhao K, et al. The role of oxidative stress in intervertebral disc degeneration: Mechanisms and therapeutic implications. Ageing Res Rev. 2024. https://doi.org/10.1016/j.arr.2024.102323. 07/01/ 2024;98:102323.
13. Broz P, Dixit VM. Inflammasomes: mechanism of assembly, regulation and signalling. Nat Rev Immunol. 2016;07(7):407–20. 10.1038/nri.2016.58. /01 2016.
14. Hornung V, Ablasser A, Charrel-Dennis M et al. AIM2 recognizes cytosolic dsDNA and forms a caspase-1-activating inflammasome with ASC. *Nature*. 2009/03/01 2009;458(7237):514–518. 10.1038/nature07725
15. Zhao Y, Yang J, Shi J, et al. The NLRC4 inflammasome receptors for bacterial flagellin and type III secretion apparatus. Nature 2011/09/01. 2011;477(7366):596–600. 10.1038/nature10510.
16. Shi J, Zhao Y, Wang Y, et al. Inflammatory caspases are innate immune receptors for intracellular LPS. Nature 2014/10/01. 2014;514(7521):187–92. 10.1038/nature13683.
17. Shi J, Zhao Y, Wang K et al. Cleavage of GSDMD by inflammatory caspases determines pyroptotic cell death. Nature. 2015/10/01 2015;526(7575):660–5. 10.1038/nature15514
18. Kayagaki N, Stowe IB, Lee BL et al. Caspase-11 cleaves gasdermin D for non-canonical inflammasome signalling. Nature. 2015/10/01 2015;526(7575):666–71. 10.1038/nature15541
19. Devant P, Boršić E, Ngwa EM, et al. Gasdermin D pore-forming activity is redox-sensitive. Cell Rep Jan. 2023;31(1):112008. 10.1016/j.celrep.2023.112008.
20. Zhao K, An R, Xiang Q, et al. Acid-sensing ion channels regulate nucleus pulposus cell inflammation and pyroptosis via the NLRP3 inflammasome in intervertebral disc degeneration. Cell Prolif Jan. 2021;54(1):e12941. 10.1111/cpr.12941.
21. Sun K, Jiang J, Wang Y, et al. The role of nerve fibers and their neurotransmitters in regulating intervertebral disc degeneration. Ageing Res Rev Nov. 2022;81:101733. 10.1016/j.arr.2022.101733.

22. Risbud MV, Shapiro IM. Role of cytokines in intervertebral disc degeneration: pain and disc content. *Nature Reviews Rheumatology*. 2014/01/01 2014;10(1):44–56. 10.1038/nrrheum.2013.160
23. Fine N, Lively S, Séguin CA, Perruccio AV, Kapoor M, Rampersaud R. Intervertebral disc degeneration and osteoarthritis: a common molecular disease spectrum. *Nature Reviews Rheumatology*. 2023/03/01 2023;19(3):136–152. 10.1038/s41584-022-00888-z
24. Sun K, Shi Y, Yan C, et al. Glycolysis-Derived Lactate Induces ACSL4 Expression and Lactylation to Activate Ferroptosis during Intervertebral Disc Degeneration. Adv Sci (Weinh) Jun. 2025;12(21):e2416149. 10.1002/advs.202416149.
25. Jia S, Gao X, Zhu L, et al. ACSL4-Dependent Lysosomal Lipid Peroxidation Links WTAP-Mediated m(6)A Modification to Intervertebral Disc Degeneration. Adv Sci (Weinh). Aug 2026;29:e77401. 10.1002/advs.77401.
26. Tu J, Li W, Yang S, et al. Single-Cell Transcriptome Profiling Reveals Multicellular Ecosystem of Nucleus Pulposus during Degeneration Progression. Adv Sci (Weinh) Jan. 2022;9(3):e2103631. 10.1002/advs.202103631.
27. Wu D, Yan C, Han L, et al. Targeted Inhibition of cGAS/STING signaling induced by aberrant R-Loops in the nucleus pulposus to alleviate cellular senescence and intervertebral disc degeneration. J Nanobiotechnology Jul. 2025;14(1):510. 10.1186/s12951-025-03579-5.
28. Chen KW, Broz P. Gasdermins as evolutionarily conserved executors of inflammation and cell death. *Nature Cell Biology*. 2024/09/01 2024;26(9):1394–1406. 10.1038/s41556-024-01474-z
29. Sun K, Yan C, Dai X, et al. Catalytic Nanodots-Driven Pyroptosis Suppression in Nucleus Pulposus for Antioxidant Intervention of Intervertebral Disc Degeneration. Adv Mater May. 2024;36(19):e2313248. 10.1002/adma.202313248.
30. Wan C, Hu M, Peng X, et al. Novel multifunctional dexamethasone carbon dots synthesized using the one-pot green method for anti-inflammatory, osteogenesis, and osteoimmunomodulatory in bone regeneration. Biomater Sci Oct. 2022;25(21):6291–306. 10.1039/d2bm01153k.
31. Wan J, Xu S, Li J, et al. Facile synthesis of multifunctional pharmaceutical carbon dots for targeted bioimaging and chemotherapy of tumors. Nanoscale Aug. 2022;11(31):11359–68. 10.1039/d2nr03321f.
32. Dehvari K, Chiu SH, Lin JS, Girma WM, Ling YC, Chang JY. Heteroatom doped carbon dots with nanoenzyme like properties as theranostic platforms for free radical scavenging, imaging, and chemotherapy. Acta Biomater Sep. 2020;15:114:343–57. 10.1016/j.actbio.2020.07.022.
33. Hu C-MJ, Fang RH, Wang K-C et al. Nanoparticle biointerfacing by platelet membrane cloaking. Nature. 2015/10/01 2015;526(7571):118–21. 10.1038/nature15373
34. He Y, Li R, Liang J, et al. Drug targeting through platelet membrane-coated nanoparticles for the treatment of rheumatoid arthritis. Nano Res. 2018;11(11):6086–101. 10.1007/s12274-018-2126-5.
35. Zhao L, Liang K, Cheng W et al. A multifaceted strategy for intra- and extracellular nucleic acid regulation to alleviate intervertebral disc degeneration. *Nature Communications*. 2025/08/26 2025;16(1):7936. 10.1038/s41467-025-63194-8

36. Dehaini D, Wei X, Fang RH, et al. Erythrocyte-Platelet Hybrid Membrane Coating for Enhanced Nanoparticle Functionalization. Adv Mater Apr. 2017;29(16). 10.1002/adma.201606209.
37. Ma M, Zhang C, Zhong Z, et al. siRNA incorporated in slow-release injectable hydrogel continuously silences DDIT4 and regulates nucleus pulposus cell pyroptosis through the ROS/TXNIP/NLRP3 axis to alleviate intervertebral disc degeneration. Bone Joint Res May. 2024;21(5):247–60. 10.1302/2046-3758.135.Bjr-2023-0320.R1.
38. Ma H, Xie C, Chen Z, et al. MFG-E8 alleviates intervertebral disc degeneration by suppressing pyroptosis and extracellular matrix degradation in nucleus pulposus cells via Nrf2/TXNIP/NLRP3 axis. Cell Death Discov Apr. 2022;19(1):209. 10.1038/s41420-022-01002-8.
39. Chen Y, Cao X, Pan B, et al. Verapamil attenuates intervertebral disc degeneration by suppressing ROS overproduction and pyroptosis via targeting the Nrf2/TXNIP/NLRP3 axis in four-week puncture-induced rat models both in vivo and in vitro. Int Immunopharmacol Oct. 2023;123:110789. 10.1016/j.intimp.2023.110789.
40. Li S, Liao Z, Luo R, et al. Autophagy-Based Unconventional Secretory for AIM2 Inflammasome Drives DNA Damage Resistance During Intervertebral Disc Degeneration. Front Cell Dev Biol. 2021;9:672847. 10.3389/fcell.2021.672847.
41. Yao Q, Lei Y, Zhang Y, et al. EZH2-H3K27me3-Mediated Epigenetic Silencing of DKK1 Induces Nucleus Pulposus Cell Pyroptosis in Intervertebral Disc Degeneration by Activating NLRP3 and NAIP/NLRC4. Inflammation Apr. 2025;48(2):902–18. 10.1007/s10753-024-02096-1.
42. Coll RC, Schroder K. Inflammasome components as new therapeutic targets in inflammatory disease. Nat Rev Immunol. 2025;01(1):22–41. 10.1038/s41577-024-01075-9. /01 2025.
43. He D, Zhou M, Bai Z, Wen Y, Shen J, Hu Z. Propionibacterium acnes induces intervertebral disc degeneration by promoting nucleus pulposus cell pyroptosis via NLRP3-dependent pathway. Biochem Biophys Res Commun Jun. 2020;4(3):772–9. 10.1016/j.bbrc.2020.03.161.
44. Zhou Y, Chen Z, Yang X, et al. Morin attenuates pyroptosis of nucleus pulposus cells and ameliorates intervertebral disc degeneration via inhibition of the TXNIP/NLRP3/Caspase-1/IL-1β signaling pathway. Biochem Biophys Res Commun Jun. 2021;25:559:106–12. 10.1016/j.bbrc.2021.04.090.
45. Tang P, Gu JM, Xie ZA, et al. Honokiol alleviates the degeneration of intervertebral disc via suppressing the activation of TXNIP-NLRP3 inflammasome signal pathway. Free Radic Biol Med. May 2018;20:120:368–79. 10.1016/j.freeradbiomed.2018.04.008.
46. Liu Y, Zhang L, Cai H, et al. Biomass-derived carbon dots with pharmacological activity for biomedicine: Recent advances and future perspectives. Sci Bull (Beijing) Oct. 2024;15(19):3127–49. 10.1016/j.scib.2024.08.011.
47. Sahana S, Gautam A, Singh R, Chandel S. A recent update on development, synthesis methods, properties and application of natural products derived carbon dots. Nat Prod Bioprospect Nov. 2023;13(1):51. 10.1007/s13659-023-00415-x.
48. Zhou H, He J, Liu R, et al. Microenvironment-responsive metal-phenolic network release platform with ROS scavenging, anti-pyroptosis, and ECM regeneration for intervertebral disc degeneration.

Bioact Mater Jul. 2024;37:51–71. 10.1016/j.bioactmat.2024.02.036.

49. Wang S, Duan Y, Zhang Q, et al. Drug Targeting via Platelet Membrane-Coated Nanoparticles. Small Struct Oct. 2020;1(1). 10.1002/sstr.202000018.
50. Han H, Bártolo R, Li J, Shahbazi MA, Santos HA. Biomimetic platelet membrane-coated nanoparticles for targeted therapy. Eur J Pharm Biopharm Mar. 2022;172:1–15. 10.1016/j.ejpb.2022.01.004.
51. Jain C, Huang JJ, Lee Y, et al. Animal Models of Disc Degeneration Using Puncture Injury: A 20 Year Perspective. JOR Spine Sep. 2025;8(3):e70093. 10.1002/jsp2.70093.
52. Poletto DL, Crowley JD, Tanglay O, Walsh WR, Pelletier MH. Preclinical in vivo animal models of intervertebral disc degeneration. Part 1: A systematic review. JOR Spine Mar. 2023;6(1):e1234. 10.1002/jsp2.1234.
53. Marinho A, Reis S, Nunes C. On the design of cell membrane-coated nanoparticles to treat inflammatory conditions. Nanoscale Horiz Dec. 2024;16(1):38–55. 10.1039/d4nh00457d.
54. Lan T, Zheng YC, Li ND, Chen XS, Shen Z, Yan B. CRISPR/dCas9-Mediated Parkin Inhibition Impairs Mitophagy and Aggravates Apoptosis of Rat Nucleus Pulposus Cells Under Oxidative Stress. Front Mol Biosci. 2021;8:674632. 10.3389/fmolb.2021.674632.
55. Jiang C, Sun ZM, Zhu DC, et al. Inhibition of Rac1 activity by NSC23766 prevents cartilage endplate degeneration via Wnt/β-catenin pathway. J Cell Mol Med. Mar 2020;24(6):3582–92. 10.1111/jcmm.15049.
56. Mendoza R, Banerjee I, Manna D, Reghupaty SC, Yetirajam R, Sarkar D. Mouse Bone Marrow Cell Isolation and Macrophage Differentiation. Methods Mol Biol. 2022;2455:85–91. 10.1007/978-1-0716-2128-8_8.
57. Huang S, Xu L, Sun Y, Wu T, Wang K, Li G. An improved protocol for isolation and culture of mesenchymal stem cells from mouse bone marrow. J Orthop Translat Jan. 2015;3(1):26–33. 10.1016/j.jot.2014.07.005.

Figures

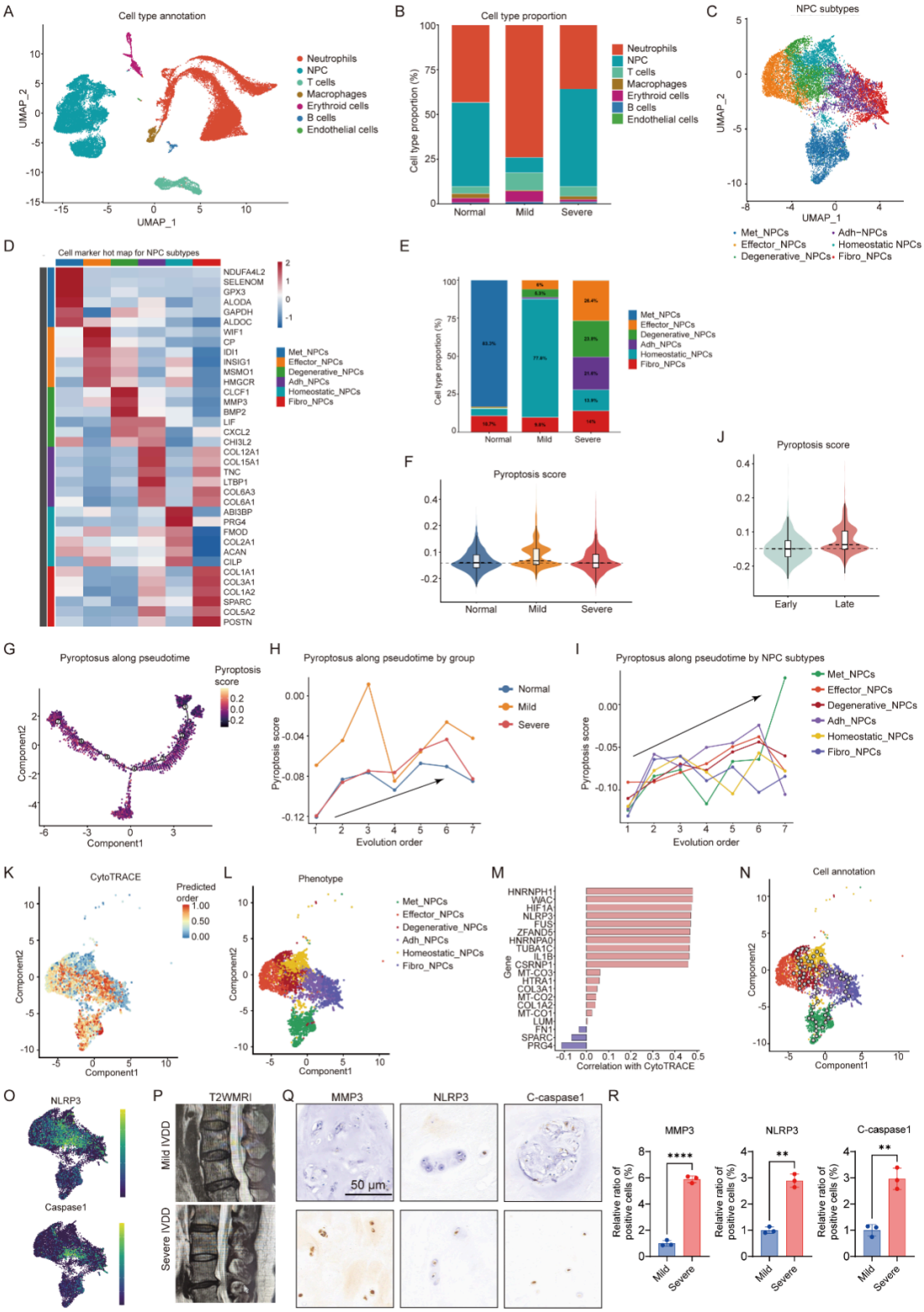


Figure 1

Single-cell transcriptomic analysis reveals NPC state remodeling and enhanced pyroptosis-associated programs during IVDD progression. (A) UMAP visualization of the major cell populations identified in human nucleus pulposus tissues by single-cell RNA sequencing, including neutrophils, nucleus pulposus cells (NPCs), T cells, macrophages, erythroid cells, B cells, and endothelial cells. (B) Relative proportions of the major cell populations across normal, mildly degenerated, and severely degenerated groups. (C)

UMAP visualization of NPC subclusters identified according to their transcriptional profiles. NPCs were classified into six subpopulations: Met_NPCs, Effector_NPCs, Degenerative_NPCs, Adh_NPCs, Homeostatic_NPCs, and Fibro_NPCs. (D) Heatmap showing representative marker genes of the six NPC subpopulations. (E) Relative proportions of the six NPC subpopulations across normal, mildly degenerated, and severely degenerated groups. (F) Violin plots showing pyroptosis scores of NPCs across the three degeneration groups. (G) Distribution of pyroptosis scores along the inferred pseudotime trajectory of NPC state transition. Cells are colored according to their pyroptosis scores. (H) Dynamic changes in pyroptosis scores along pseudotime in NPCs from normal, mildly degenerated, and severely degenerated groups. (I) Dynamic changes in pyroptosis scores along pseudotime among the six NPC subpopulations. (J) Comparison of pyroptosis scores between early- and late-state NPCs along the inferred pseudotime trajectory. (K) CytoTRACE analysis showing the predicted differentiation order of NPCs, with higher CytoTRACE scores indicating greater developmental potential. (L) Distribution of the six NPC subpopulations on the CytoTRACE-derived cellular-state map. (M) Genes positively or negatively correlated with CytoTRACE scores, indicating genes associated with NPC state progression. (N) Distribution and annotation of NPC subpopulations along the inferred cellular-state transition trajectory. (O) Feature plots showing the expression distribution of the pyroptosis-associated genes NLRP3 and CASP1 across NPC states. (P) Representative T2-weighted MRI images of mildly and severely degenerated human intervertebral discs. (Q) Representative immunohistochemical staining of MMP3, NLRP3, and cleaved Caspase-1 in mildly and severely degenerated human intervertebral disc tissues. Scale bar, 50 μm. (R) Quantification of MMP3-, NLRP3-, and cleaved-Caspase-1-positive cells in mildly and severely degenerated intervertebral disc tissues (n = 3). Data are presented as mean ± SD. **P < 0.01 and ****P < 0.0001.

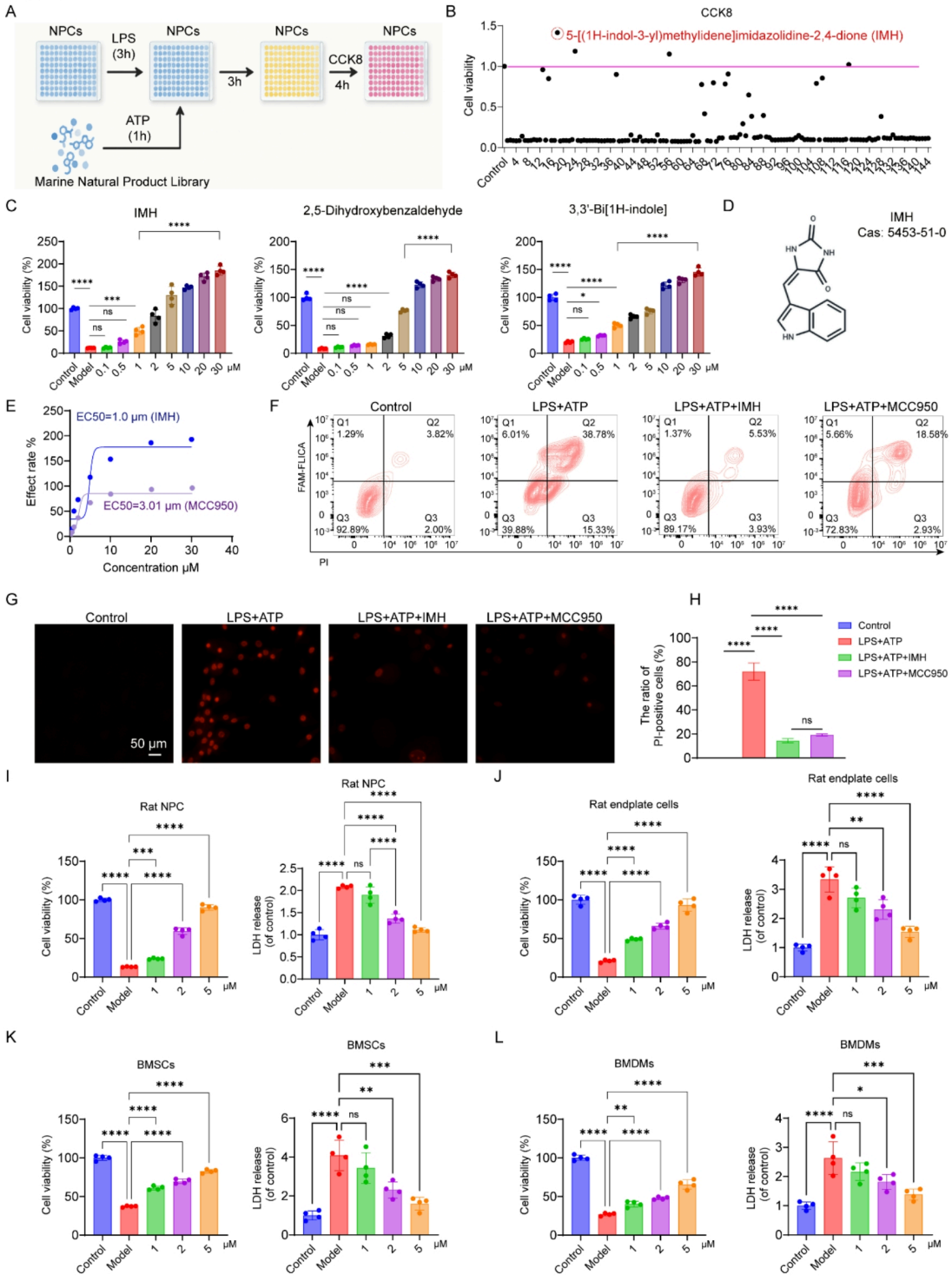
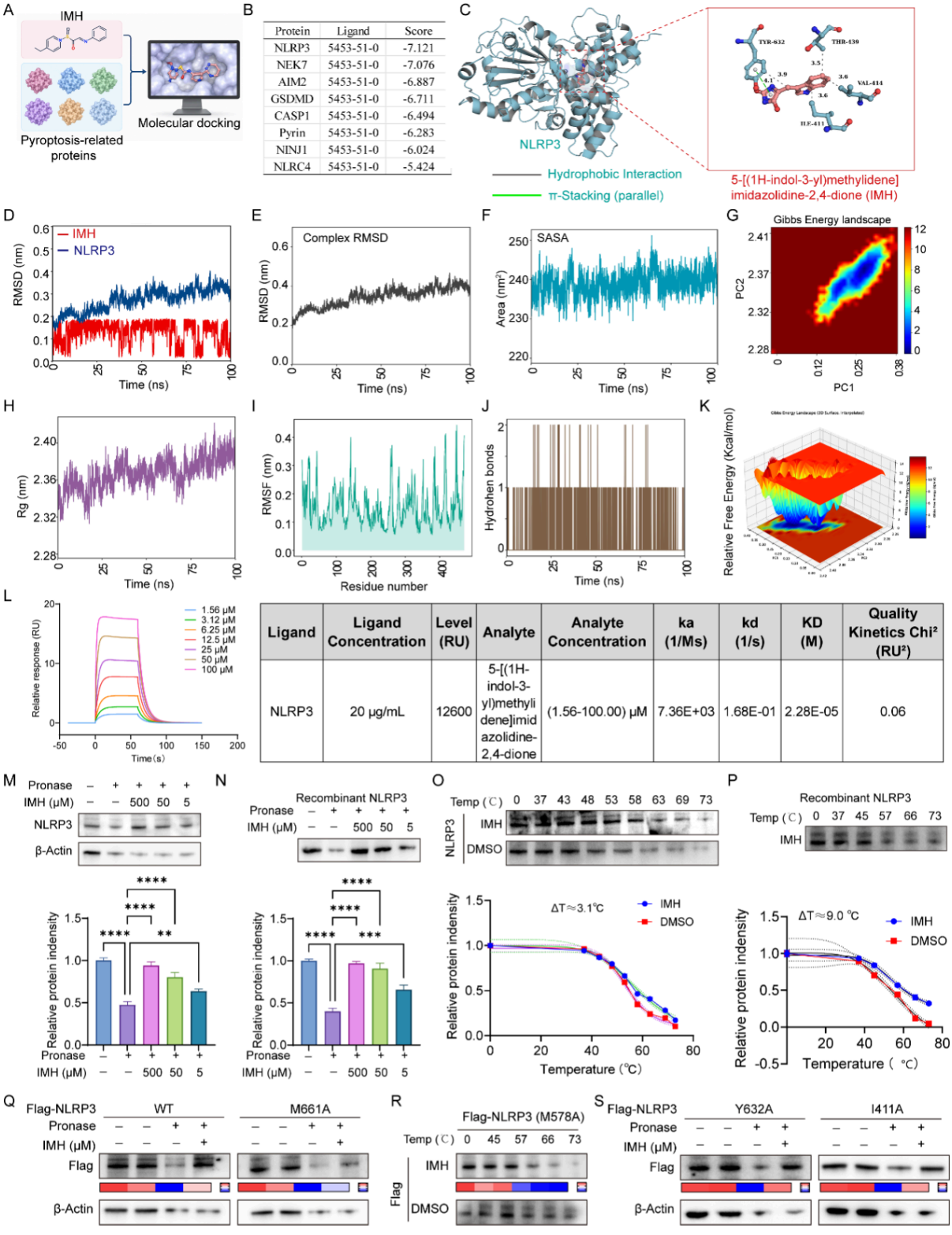


Figure 2

Marine natural product screening identifies IMH as an NLRP3-associated anti-pyroptotic compound (A) Schematic workflow of phenotype-based screening of marine natural products using an LPS/ATP-induced NPC pyroptosis model. (B) CCK-8-based primary screening of marine natural products for protective effects against LPS/ATP-induced NPC injury. (C) Concentration-dependent effects of IMH, 2,5-dihydroxybenzaldehyde, and 3,3'-bi(1H-indole) on NPC viability following LPS/ATP stimulation (n=4). (D)

Chemical structure of IMH (CAS No. 5453-51-0). (E) Concentration–response curves and apparent EC50 values of IMH and MCC950 in LPS/ATP-stimulated NPCs. (F) Flow cytometric analysis of pyroptotic cells by FAM-FLICA/PI double staining following the indicated treatments. (G) Representative PI fluorescence images showing loss of plasma membrane integrity following the indicated treatments. (H) Quantification of PI-positive cells (n=3). (I-L) Concentration-dependent effects of IMH on cell viability and LDH release in rat NPCs, rat endplate cells, bone marrow-derived mesenchymal stem cells (BMSCs), and bone marrow-derived macrophages (BMDMs) following inflammasome-associated stimulation (n=4).



Protein	Ligand	Score
NLRP3	5453-51-0	-7.121
NEK7	5453-51-0	-7.076
AIM2	5453-51-0	-6.887
GSDMD	5453-51-0	-6.711
CASP1	5453-51-0	-6.494
Pyrin	5453-51-0	-6.283
NINJ1	5453-51-0	-6.024
NLRC4	5453-51-0	-5.424

Ligand	Ligand Concentration	Level (RU)	Analyte	Analyte Concentration	ka (1/Ms)	kd (1/s)	KD (M)	Quality Kinetics Chi² (RU²)
NLRP3	20 μg/mL	12600	5-[(1H-indol-3-yl)methylidene]imidazolidine-2,4-dione	(1.56-100.00) μM	7.36E+03	1.68E-01	2.28E-05	0.06

Figure 3

Multidimensional target validation identifies NLRP3 as a direct molecular target of IMH (A) Schematic workflow of molecular docking of IMH against pyroptosis-related proteins. (B) Predicted docking scores of IMH with NLRP3, NEK7, AIM2, GSDMD, CASP1, Pyrin, NINJ1, and NLRC4. (C) Predicted binding conformation of IMH within the NLRP3 binding pocket and representative non-covalent interactions with surrounding residues, including hydrophobic interactions and π-π stacking. (D-K) Molecular dynamics analysis of the IMH-NLRP3 complex during a 100-ns simulation. (D) RMSD profiles of IMH and NLRP3. (E) RMSD of the IMH–NLRP3 complex. (F) Solvent-accessible surface area (SASA). (G) Two-dimensional Gibbs free-energy landscape based on principal component analysis. (H) Radius of gyration (Rg). (I) Per-residue root mean square fluctuation (RMSF). (J) Number of hydrogen bonds formed during the simulation. (K) Three-dimensional Gibbs free-energy landscape of the IMH-NLRP3 complex. (L) Surface plasmon resonance (SPR) analysis of IMH binding to recombinant NLRP3, showing concentration-dependent sensorgrams and kinetic parameters. (M) DARTS analysis of endogenous NLRP3 showing IMH-dependent protection against Pronase-mediated proteolysis, with corresponding quantification (n=3). (N) DARTS analysis using recombinant NLRP3 protein, with corresponding quantification (n=3). (O) Cellular thermal shift assay (CETSA) of endogenous NLRP3 showing IMH-induced thermal stabilization and the corresponding thermal shift curve. (P) CETSA analysis of recombinant NLRP3 showing IMH-induced thermal stabilization. (Q) DARTS analysis comparing IMH-induced stabilization of wild-type NLRP3 and the M661A mutant. (R) CETSA analysis of the NLRP3 M578A mutant. (S) DARTS analysis of the NLRP3 Y632A and I411A mutants.

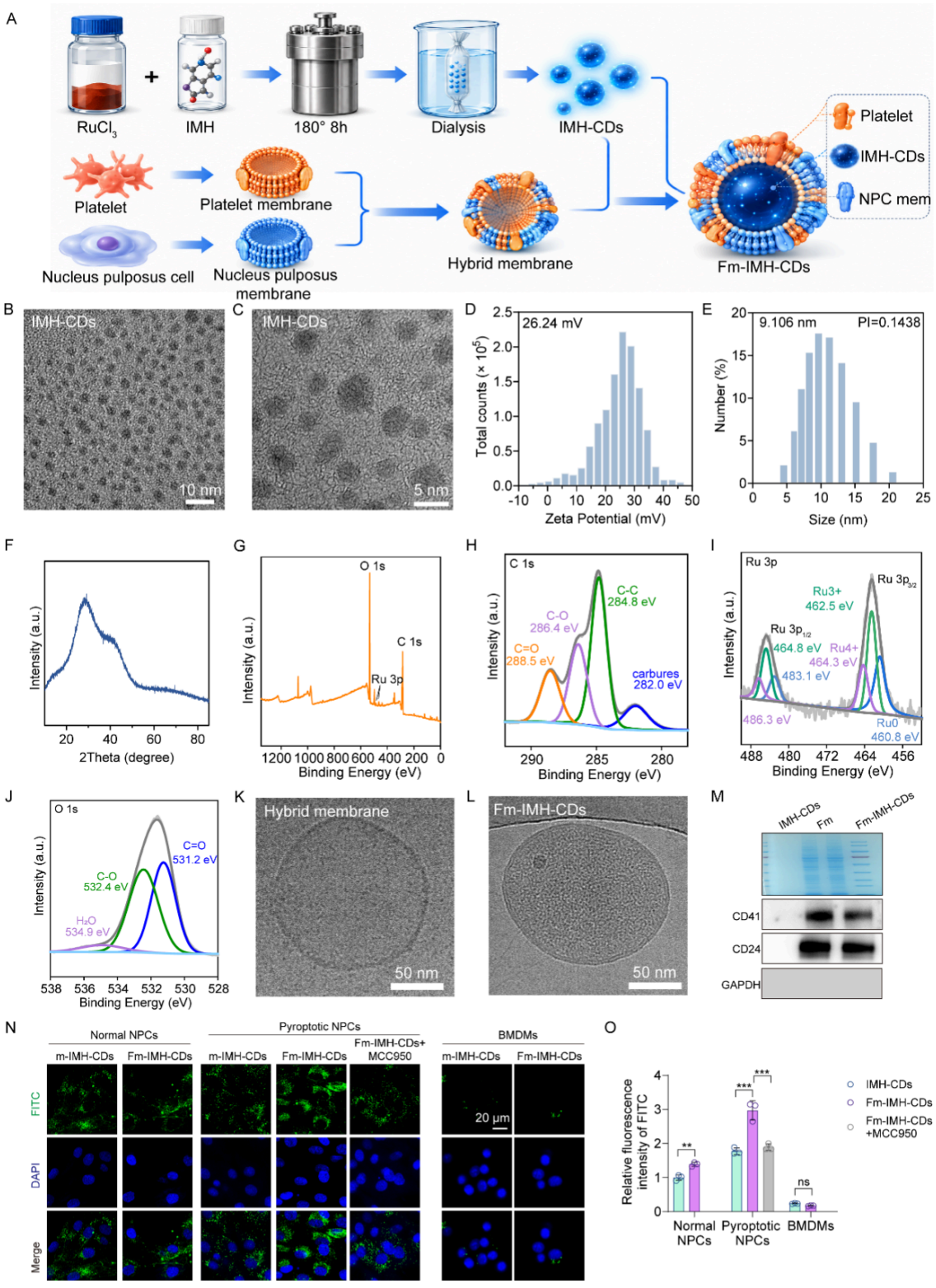


Figure 4

Preparation and characterization of Fm-IMH-CDs. (A) Schematic illustration of the synthesis of Ru-containing IMH-derived carbon dots and subsequent platelet/NPC hybrid-membrane coating to generate Fm-IMH-CDs. (B, C) Representative TEM images of IMH-CDs. (D, E) Zeta potential and particle-size distribution of IMH-CDs, respectively. (F) XRD pattern of IMH-CDs. (G) XPS survey spectrum of IMH-CDs. (H-J) High-resolution C 1s, Ru 3p, and O 1s XPS spectra, respectively. (K, L) Representative cryo-TEM

images of the platelet/NPC hybrid membrane and Fm-IMH-CDs, respectively. (M) Coomassie brilliant blue staining and Western blot analysis of the platelet marker CD41 and NPC-associated marker CD24, confirming retention of membrane proteins from both source cells in Fm-IMH-CDs. (N) Representative fluorescence images showing the cellular association of m-IMH-CDs and Fm-IMH-CDs with normal NPCs, pyroptotic NPCs, and BMDMs, as well as the effect of MCC950 pretreatment on Fm-IMH-CD association with pyroptotic NPCs. (O) Quantification of the relative FITC fluorescence intensity in the indicated groups.

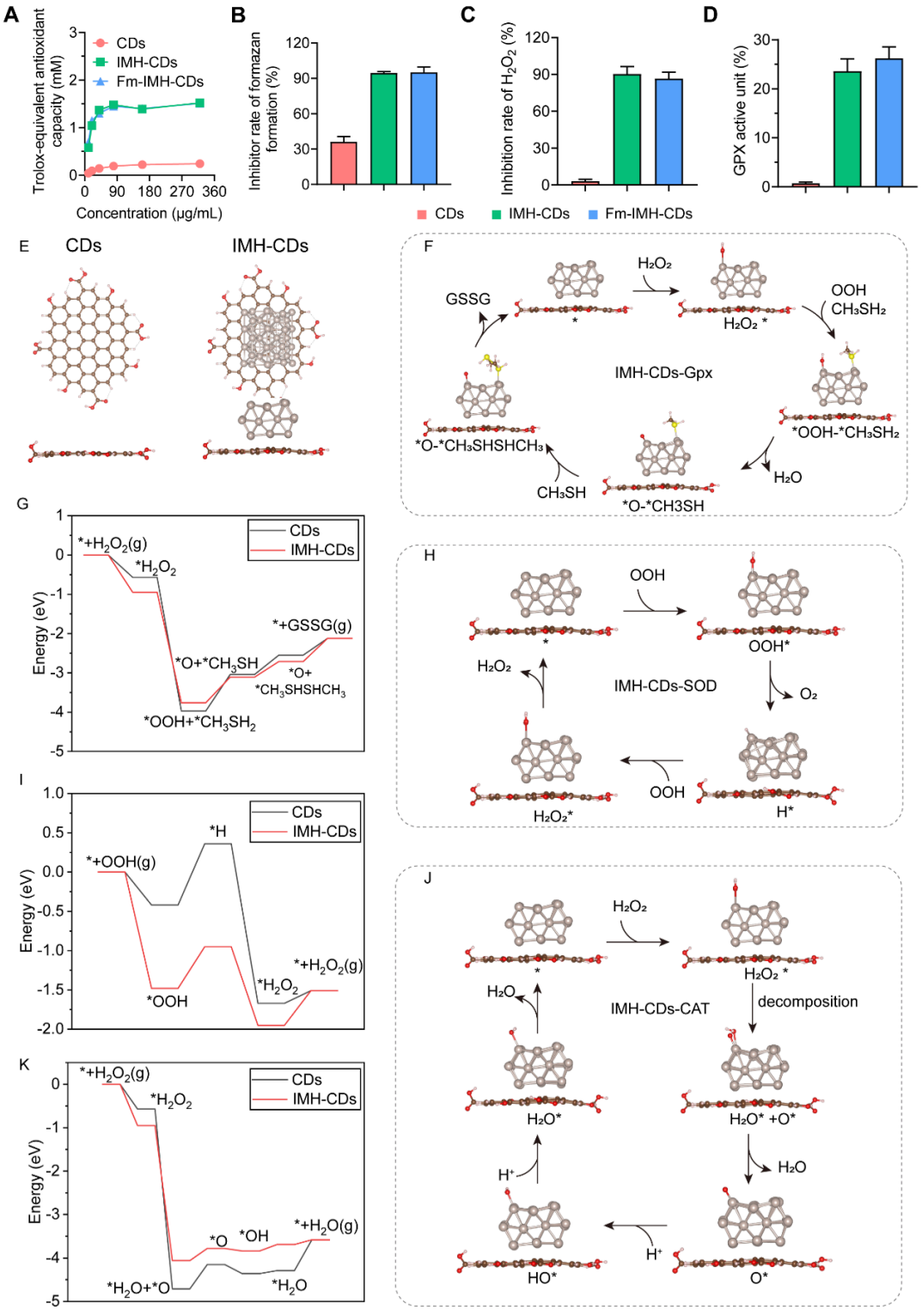


Figure 5

Enzyme-mimetic activities and mechanistic analysis of Fm-IMH-CDs. (A) Trolox-equivalent antioxidant capacity of CDs, IMH-CDs, and Fm-IMH-CDs. (B) SOD-like activity of the indicated formulations. (C) CAT-like activity of the indicated formulations. (D) GPx-like activity of the indicated formulations. (E) Structural models of Ru-free CDs and Ru-containing IMH-CDs. (F, G) Proposed GPx-like catalytic pathway of IMH-CDs and the corresponding calculated energy profile. (H, I) Proposed SOD-like catalytic pathway of IMH-CDs and the corresponding calculated energy profile. (J, K) Proposed CAT-like catalytic pathway of IMH-CDs and the corresponding calculated energy profile.

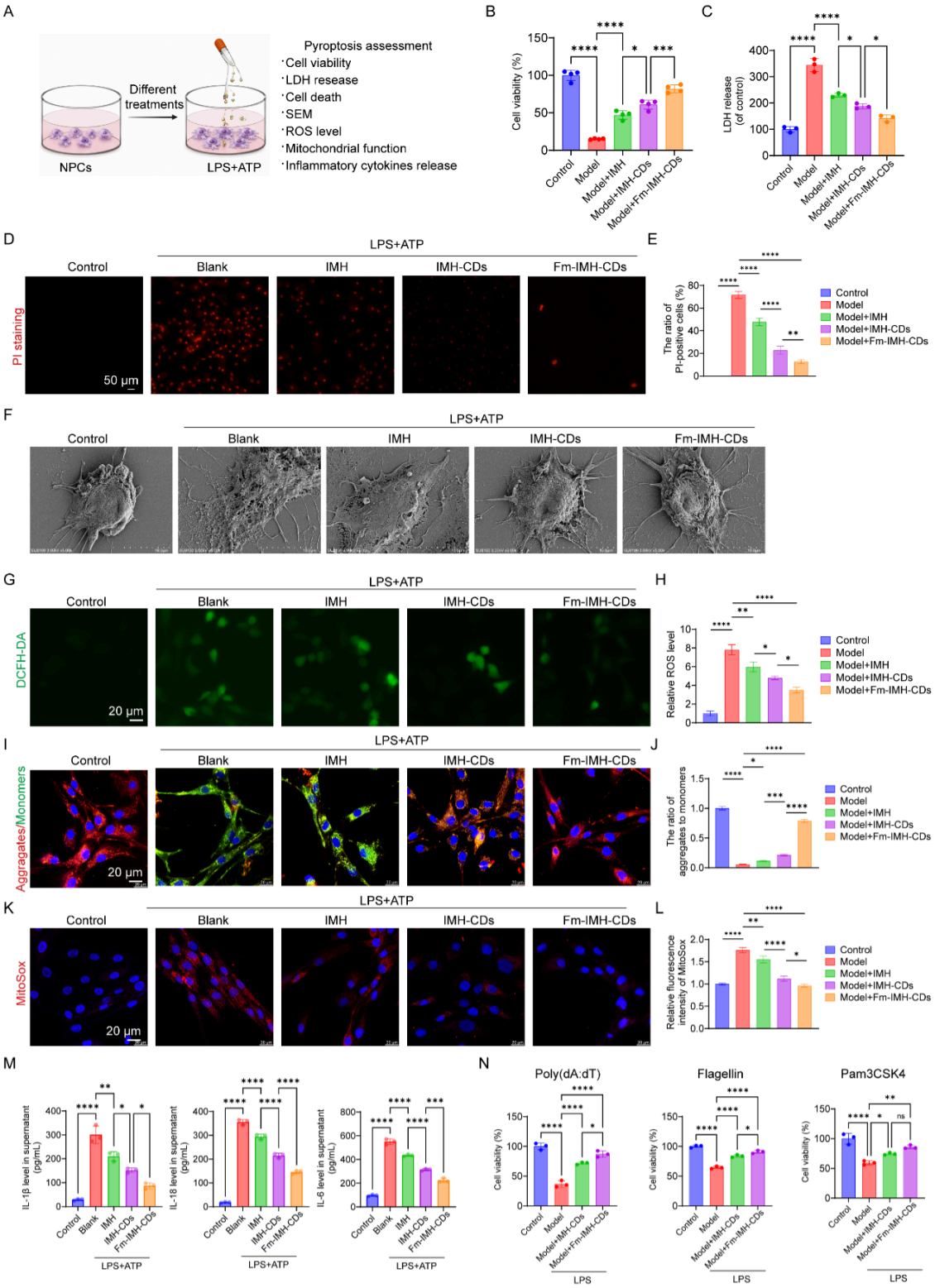


Figure 6

Fm-IMH-CDs provide multidimensional protection against pyroptosis-associated cellular injury by regulating oxidative stress and mitochondrial dysfunction. (A) Schematic illustration of the in vitro experimental design for evaluating pyroptosis-associated injury in NPCs. (B) Cell viability of NPCs in the Control, Model, Model + IMH, Model + IMH-CDs, and Model + Fm-IMH-CDs groups assessed by CCK-8 assay. (C) LDH release from NPCs after the indicated treatments. (D) Representative PI fluorescence

images showing loss of plasma membrane integrity. Scale bar, 50 μm. (E) Quantification of PI-positive cells. (F) Representative SEM images showing pyroptosis-associated changes in cell-surface morphology. (G) Representative DCFH-DA fluorescence images showing intracellular ROS levels. Scale bar, 20 μm. (H) Quantification of relative intracellular ROS levels. (I) Representative JC-1 fluorescence images showing mitochondrial membrane potential. Scale bar, 20 μm. (J) Quantification of the JC-1 aggregate-to-monomer fluorescence ratio. (K) Representative MitoSOX fluorescence images showing mitochondrial ROS (mtROS) levels. Scale bar, 20 μm. (L) Quantification of relative MitoSOX fluorescence intensity. (M) Levels of IL-1β, IL-18, and IL-6 in culture supernatants. (N) Cell viability under LPS + ATP, poly(dA:dT), flagellin, and Pam3CSK4 stimulation following treatment with IMH-CDs or Fm-IMH-CDs, as assessed by the CCK-8 assay. Statistical significance is indicated as ns, not significant; *P < 0.05, **P < 0.01, ***P < 0.001, and ****P < 0.0001.

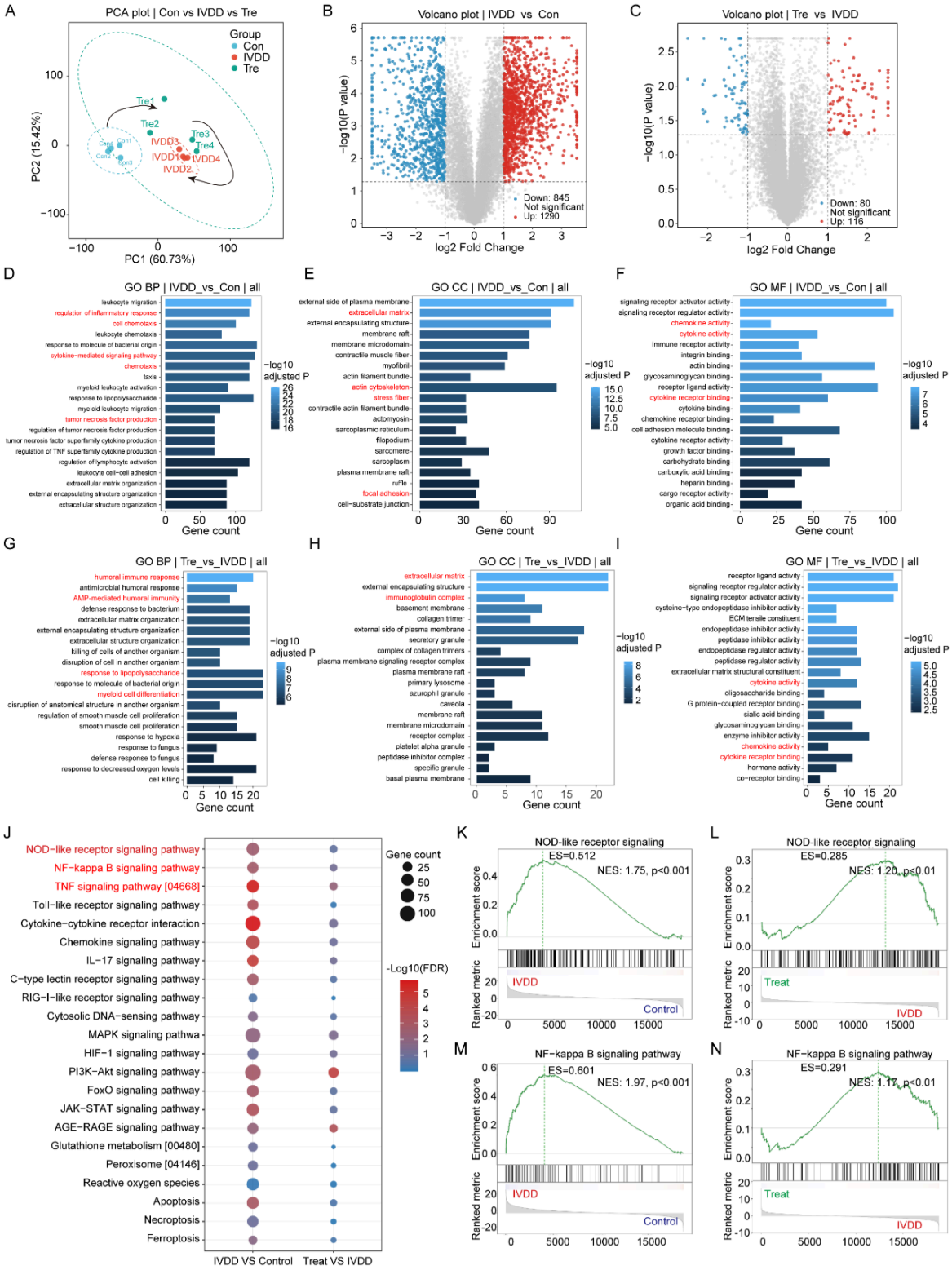


Figure 7

Transcriptomic profiling reveals that Fm-IMH-CDs remodel IVDD-associated inflammatory and immune transcriptional networks. (A) Principal component analysis (PCA) of transcriptomic profiles from the Control (Con), IVDD, and Fm-IMH-CD-treated (Tre/Treat) groups. **(B)** Volcano plot of differentially expressed genes between the IVDD and Control groups. A total of 1,290 genes were upregulated and 845 genes were downregulated in the IVDD group. **(C)**Volcano plot of differentially expressed genes

between the Treat and IVDD groups, showing 116 upregulated and 80 downregulated genes following treatment. **(D-F)** Gene Ontology (GO) enrichment analysis of differentially expressed genes between the IVDD and Control groups, including biological process (BP; D), cellular component (CC; E), and molecular function (MF; F). **(G-I)** GO enrichment analysis of differentially expressed genes between the Treat and IVDD groups, including BP (G), CC (H), and MF (I). **(J)** KEGG pathway enrichment analysis of differentially expressed genes from the IVDD versus Control and Treat versus IVDD comparisons. **(K)** Gene set enrichment analysis (GSEA) of the NOD-like receptor signaling pathway in IVDD versus Control. **(L)** GSEA of the NOD-like receptor signaling pathway in Treat versus IVDD. **(M)** GSEA of the NF-κB signaling pathway in IVDD versus Control. **(N)** GSEA of the NF-κB signaling pathway in Treat versus IVDD.

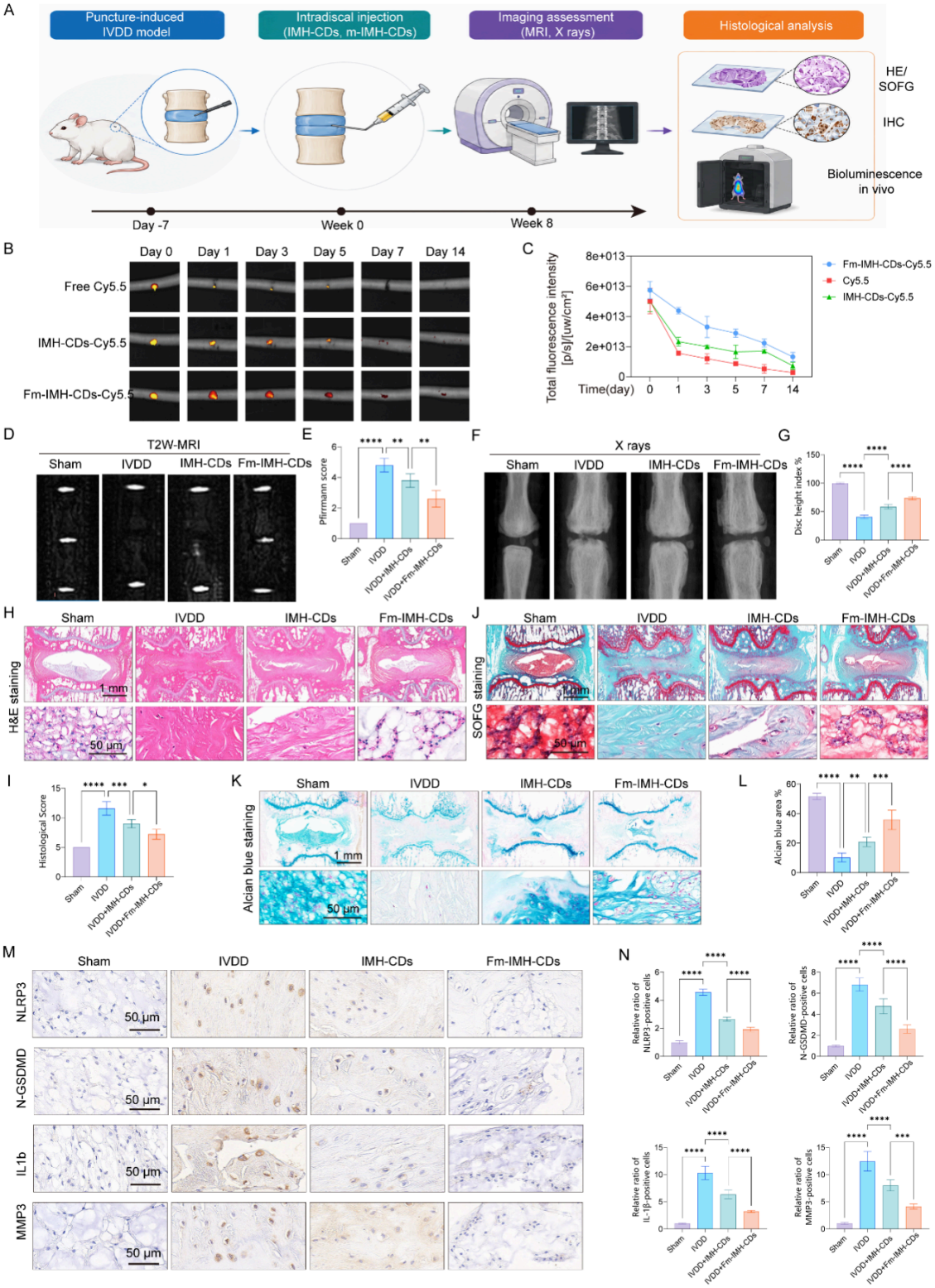


Figure 8

Fm-IMH-CDs prolong intradiscal retention and attenuate IVDD progression and pyroptosis-associated inflammation in vivo. (A) Schematic illustration of the puncture-induced rat IVDD model, intradiscal administration of IMH-CDs or Fm-IMH-CDs, in vivo imaging, radiological assessment, and subsequent histological analyses. (B) Representative in vivo fluorescence images at days 0, 1, 3, 5, 7, and 14 after intradiscal administration of free Cy5.5, Cy5.5-labeled IMH-CDs, or Cy5.5-labeled Fm-IMH-CDs. (C)

Quantification of total fluorescence intensity in the intervertebral disc region at the indicated time points. (D) Representative T2-weighted magnetic resonance imaging (MRI) images of intervertebral discs from the Sham, IVDD, IVDD + IMH-CDs, and IVDD + Fm-IMH-CDs groups. (E) Quantification of Pfirrmann degeneration scores. (F) Representative X-ray images of intervertebral discs from the indicated groups. (G) Quantification of the disc height index (DHI). (H) Representative hematoxylin and eosin (H&E) staining of intervertebral disc tissues from the indicated groups. Scale bars, 1 mm and 50 μm. (I) Quantification of histological degeneration scores. (J) Representative Safranin O/Fast Green (SOFG) staining showing intervertebral disc architecture and proteoglycan-rich extracellular matrix. Scale bars, 1 mm and 50 μm. (K) Representative Alcian blue staining of intervertebral disc tissues. Scale bars, 1 mm and 50 μm. (L) Quantification of the Alcian blue-positive matrix area. (M) Representative immunohistochemical staining of NLRP3, N-GSDMD, IL-1β, and MMP3 in intervertebral disc tissues from the indicated groups. Scale bar, 50 μm. (N) Quantification of NLRP3-, N-GSDMD-, IL-1β-, and MMP3-positive cells. Statistical significance is indicated as *P < 0.05, **P < 0.01, ***P < 0.001, and ****P < 0.0001.

Supplementary Files

This is a list of supplementary files associated with this preprint. Click to download.

- SI1.docx